Dual-reaction center catalyst based on common metals Cu-Mg-Al for synergistic peroxymonosulfate adsorption-activation in Fenton-like process

Zhiqun Xie [a], Dionysios D. Dionysiou [b], Shuang Luo [a,c], Menglin Chen [a], Zongsu Wei [a,*]

[a] *Center for Water Technology (WATEC) & Department of Biological and Chemical Engineering, Aarhus University, Universitetsbyen 36, Aarhus C 8000, Denmark*
[b] *Environmental Engineering and Science Program, Department of Chemical and Environmental Engineering (ChEE), University of Cincinnati, Cincinnati, OH 45221, USA*
[c] *College of Resources and Environment, Hunan Agricultural University, Changsha 410128, China*

ABSTRACT

To improve the peroxymonosulfate (PMS) utilization and the catalyst stability, a dual-reaction center catalyst, $Cu-Mg_{0.388}Al_{2.408}O_4$-BN, was fabricated free of expensive rare metals. The presence of Mg leads to a positive-charged surface that was highly favorable for adsorbing bisphenol A (BPA) and PMS anions under neutral pH conditions. The relatively low electronegativity of Mg, together with the electronic compensation of cation-π between Cu and boron nitride (BN), resulted in the formation of the electron-rich Cu center. The combination of the electrostatic attraction and dual-reaction center led to the rapid degradation of BPA via a fast electron transfer step from BPA to the electron-rich Cu center, and then to PMS for effective activation. This unique design renders excellent reusability and stability of the catalyst by avoiding the redox cycle of Cu(I)/Cu(II). This research work opens new horizons to use common metals for efficient activation of PMS as economical alternatives over expensive rare metal catalysts in Fenton-like processes.

1. Introduction

Advanced oxidation processes (AOPs) can eliminate toxic and persistent organic pollutants via in-situ generation of highly potent reactive oxygen species (ROS), such as hydroxyl radicals (•OH) from hydrogen peroxide (H_2O_2) and sulfate radicals ($SO_4^{\bullet-}$) from peroxymonosulfate (PMS) activation [1,2]. Compared to H_2O_2, PMS is more stable for safer transportation and storage. $SO_4^{\bullet-}$ has a comparable oxidation potential (2.5–3.1 V) to that of •OH (2.7 V) but a longer life (30–40 μs) than •OH (20 ns) [3,4]; additionally, PMS activation can be operated at a wider pH range (2-8) [5]. In this context, transition metal-based catalysts (*e.g.*, Co(II) and Fe(II)) are often utilized for PMS activation, which is also called a Fenton-like reaction system [4]. However, the redox cycle of these metal elements (*e.g.*, Co(II)→Co(III)→Co(II) and Fe(II)→Fe(III)→Fe (II)) is the rate-limiting step in PMS activation [6], since the accumulation of the high valence metal will eventually hinder the catalytic reactivity [7].

To overcome the limitation of the redox cycle, the scheme of a dual-reaction center has recently been employed via constructing nonuniform distribution of electrons on the catalyst surface as an attractive alternative [8–11]. In heterogeneous Fenton catalysts, the distribution of extranuclear electrons from one atom is affected by its neighbouring atoms with different electronegativity, resulting in a polarization distribution on the catalyst surface. Such polarization difference can be enhanced by introducing different electronegative metals or metal-nonmetal combinations (e.g., cation-π interaction) to form an electron-rich center (cathode-equivalent) and electron-poor center (anode-equivalent), where oxidants and organic pollutants can be respectively reduced and oxidized [11]. This galvanic-like cell mechanism could realize efficient electron transfer from pollutant molecules to oxidants avoiding the change of metal valence [12,13]. In addition, it has been proven that the interaction between catalyst and oxidants via electrostatic adsorption will accelerate the electron transfer allowing more sufficient utilization of the oxidants [14]. Therefore, it is very appealing to construct such a dual-reaction center catalyst that not only creates surface polarization difference for directional transmission of the electron but also provides adsorption sites for PMS to utilize them effectively.

Following green chemistry principles, catalyst design with environmentally friendly and low-cost materials has become a priority. Cu-containing catalysts have gained attention due to their high abundance, low cost, and straightforward redox cycle of Cu(II)/Cu(I)

[15–18]. For instance, Lyu et al. doped Cu onto mesoporous silica microspheres and γ-Al_2O_3 to activate H_2O_2 for bisphenol A (BPA) degradation [17,18]. Notably, it was found that the phenolic hydroxyl group and the doped Cu form σ-Cu ligand complex which accelerated Cu (II)/Cu(I) cycles resulting in higher $\cdot$OH production from H_2O_2. However, the small electronegativity difference between Cu (1.90) and Al (1.61) did not induce the formation of a dual-reaction center, which led to the decline of catalytic efficiency with poor reusability in the later stage of the catalytic reaction. To address this concern, magnesium (Mg) aluminium oxides could be a better support to construct a Cu-based dual-reaction center catalyst. The presence of Mg with a lower electronegativity (1.31) may easily induce a larger polarization with Cu (1.90). Furthermore, magnesium oxide can enhance the point of zero charge (PZC) of the catalyst ($PZC_{MgO} = 12.4$, $PZC_{Al_2O_3} = 8.2$, and $PZC_{CuO} = 9.5$), and thus can promote the electrostatic adsorption ability for the electron-rich oxidants and/or negatively charged pollutants [19–21]. So far, no dual-reaction center catalyst with Cu-Mg-Al composite has been reported and the schemes are lacking to develop such common metal-based Fenton-like catalysts. Although Co-based catalysts are considered as the most efficient material for PMS activation [22], Cu-based Fenton-like catalyst is more economical and readily available. Likewise, dual-reaction center catalysts are more stable than traditional transition metal catalysts for PMS activation [23].

Inspired by this view, herein, we have prepared a novel dual reaction center catalyst, Cu-doped magnesium aluminium oxide loaded with boron nitride (BN) (Cu-$Mg_{0.388}Al_{2.408}O_4$-BN). The as-obtained catalyst free of rare metals was used to enhance PMS utilization and activation, and subsequently to degrade a model of anionic pollutants, BPA, which causes endocrine/metabolic disorders and increases the risk of cancer [24]. The introduction of the hexagonal BN, which is similar to graphene with a benzene-ring-like structure, can form cation-π interaction with Cu to promote the electron-rich Cu center formation [25]. In the meantime, its benzene-ring-like structure can interact with the benzene ring of BPA by π-π conjugation which would also facilitate the charge transfer process [26]. The activation process of PMS by Cu-$Mg_{0.388}Al_{2.408}O_4$-BN was evaluated through the optimization of the catalytic reaction conditions as well as the stability of the catalyst. Then, the formation of the electron-rich Cu center was proven by different characterization methods. Density functional theory (DFT) calculations were performed to unveil the electron distribution of the surface elements to further verify the formation of polarization difference. The correlation between adsorption ability and catalytic performance of Cu-$Mg_{0.388}Al_{2.408}O_4$-BN for PMS has been identified, providing a synergistic effect combining dual-reaction center and adsorption mechanism for BPA degradation. In addition, several principles of green chemistry were employed in this catalyst design, i.e., "Prevention" of waste production, "Safer Solvents" of water used, and "Designing Safer Chemicals" to avoid secondary contamination.

2. Experimental

2.1. Chemicals

Glucose ($C_6H_{12}O_6$), aluminium isopropoxide [$Al(OiPr)_3$] (>98%), magnesium acetate tetrahydrate [$(H_3CCOO)_2Mg\cdot4H_2O$] (99%), boron nitride (BN), copper (II) chloride dihydrate ($CuCl_2\cdot2H_2O$) (>99%), peroxymonosulfate (PMS), bisphenol A (BPA), methanol (MeOH), chloroform, *tert*-butanol (TBA), potassium iodide (KI) (99%), furfuryl alcohol (FFA) ($\geq$98.5%), nitric acid, sodium sulphate were bought from VWR Denmark. Deionized (DI) water was used during the study, having a resistivity of 18.2 MΩ $\times$ cm.

2.2. Preparation of catalysts

Cu-$Mg_{0.388}Al_{2.408}O_4$-BN was synthesized using an evaporation-induced self-assembly reaction [17], and the stoichiometry of the final

product was determined from XRD characterization. Typically, 8.4 g of $Al(OiPr)_3$, 0.4 g of ($H_3CCOO)_2Mg\cdot4H_2O$, 0.4 g of $CuCl_2\cdot2H_2O$, 7.2 g of glucose, and 0.015 g of BN were added in 100 mL DI water under stirring for 12 h at ambient temperature. Then, the mixture was transferred to a heater for further evaporation at 370 $^\circ$C under continuous stirring. The obtained solid was placed in a muffle furnace for calcination at 600 $^\circ$C for 6 h. Finally, the sample was washed using DI water and absolute ethanol three times, respectively, and then placed in an oven at 80 $^\circ$C to dry for a whole night.

To optimize the Cu doping content, we prepared composites with different Cu contents. According to the added amount of $CuCl_2\cdot2H_2O$ (0.3 g, 0.4 g and 0.5 g), the synthesized composites were named 0.3CM, 0.4CM, and 0.5CM, where CM refers to the Cu-$Mg_{0.388}Al_{2.408}O_4$ composites. In addition, Cu-$Mg_{0.388}Al_{2.408}O_4$-BN composites with various BN contents were also prepared. The added amount of 0.005 g, 0.01 g, 0.015 g, and 0.02 g BN corresponded to the samples named CM-0.005BN, CM-0.01BN, CM-0.015BN, and CM-0.02BN, respectively.

2.3. Characterization of catalysts

A field emission scanning electron microscope (AXIS-Ultra X-ray photoelectron spectroscope, Kratos SEM Nova Nano 450) and a transmission electron microscope (TecnaiTM Spirit) were used to characterize the surface morphology and structural information of Cu-$Mg_{0.388}Al_{2.408}O_4$-BN respectively, which can prove the successful synthesis of Cu-$Mg_{0.388}Al_{2.408}O_4$-BN. Micromeritics TriStar 3000 analyzer was used to measure the surface area and porosity of different samples, which are important parameters related to the adsorption performance. X-ray diffraction (XRD) spectra were analyzed to get the crystal information using XRD AERIS in the 5–90° 2θ range. The specific crystal structure can be analyzed from the XRD pattern. To study the chemical valence states of Cu-supported catalysts, X-ray photoelectron spectroscopy (XPS) analysis of samples before and after catalyst use was performed using an AXIS-Ultra X-ray photoelectron spectroscope. In addition, XPS spectra are important to prove the formation of dual-reaction center. CaseXPS was used to analyze the XPS data, a Shirley background was used for the correction. Curve-fitting employed Gaussian (20%)–Lorentzian (80%) peak-shapes (defined in CasaXPS as GL(80)). To assess the electron transfer ability of samples in different conditions and the redox properties of Cu in different samples, electrochemical impedance spectroscopy (EIS) and cyclic voltammetry (CV) analyses were performed using an electrochemical workstation (CHI760E, Shanghai, China; 50 mL 0.5 M Na_2SO_4 as the electrolyte). The electrochemical workstation is also a good tool to prove the formation of an electron-rich Cu center by analyzing the changes of reduction potential of Cu in different samples. Zeta potential was measured to analyze the electrical property of the catalyst surface, which is important to prove the positive-charged surface of the catalyst. FTIR spectra were recorded on a PerkinElmer Spectrum ONE FT-IR spectrometer in the range of 4000–400 cm^{-1} to prove the BPA and PMS adsorption. Finally, inductively coupled plasma-optical emission spectrometry (ICP-OES 4300 Optima, Perkin-Elmer) was used to determine the content of copper in different samples and the metal leaching amount after catalytic degradation reactions, an important indicator to the stability of the catalyst.

2.4. Catalytic performance

BPA degradation experiments were performed to assess the catalytic activity of as-synthesized catalysts. Typically, 10 mL of 200 mg L^{-1} (ppm) BPA was diluted into 100 mL with DI water and then 0.1 g catalysts were mixed in the solution (1 g L^{-1} catalyst, 20 mg L^{-1} BPA (87.6 μM)). The selected BPA concentration of 20 mg L^{-1} was close to the reported values in the landfill leachates and also conducive to the study of degradation kinetics and mechanism [27]. After adsorption for 30 min, 1 mL of 0.1 M PMS was added into the system (1 mM PMS). At

given time intervals, a 1 mL sample was collected, filtered through a 0.45 μm Millipore filter, and analyzed by HPLC equipped with a fluorescence detector for BPA measurements. A total organic carbon (TOC) analyzer was used to analyze the total organic carbon in solution and thus determine the mineralization of the pollutants after different reaction time intervals. In addition, to compare the utilization of PMS (η), the value of TOC removal (ΔTOC) to the actual PMS consumption ([ΔPMS]$_A$) was calculated and used as an indicator [11]. The PMS concentration that remained in the solution was determined via the KI method [28]. Furthermore, successive cyclic experiments were conducted to analyze the catalyst stability. We also used the ICP-OES to evaluate the leaching of Cu during the degradation process.

2.5. Theoretical calculations

To prove the formation of polarization difference on the surface of the catalyst based on our design, theoretical calculations can be used for analyzing the electron distribution on different elements. The theoretical calculations were conducted by Gaussian 16 A.03 program [29]. Specifically, the geometry optimization was conducted at B3LYP-D3 (BJ)/6–31 G* level. All geometries used in the studies were fully optimized and confirmed to be minimum since no imaginary frequencies were found. The single point energies of the optimized configurations were calculated at higher level of B3LYP-D3(BJ)/6–311 G* * [30]. Solvation effects were also taken into consideration with SMD model in water [31]. It is well-known that valence electron density analysis is a powerful tool to evaluate molecular electronic structure [32]. The.fch files produced from single point energy calculation were then treated by the Multiwfn program 3.8 for valence electron density analysis [33]. The adsorption energies were calculated for evaluating the interaction between the PMS/BPA and catalyst, which were defined as:

$$E_{ads} = E_{total} - E_{substrate} - E_{molecule}$$

where E_{total}, $E_{substrate}$, and $E_{molecule}$ denote the single point energy of the configurations of substrate with adsorbate, substrate, and free adsorbate molecule, respectively.

3. Result and discussion

3.1. Morphology and structure of catalysts

First, a suite of characterization methods was applied to determine the morphology and crystallinity properties of Cu-Mg$_{0.388}$Al$_{2.408}$O$_4$-BN, examine the changes before and after modification, and elucidate the electron-rich Cu center formation. Fig. 1a displays the SEM image of Cu-Mg$_{0.388}$Al$_{2.408}$O$_4$-BN which shows an irregular morphology. According to the BET analysis, this irregular morphology yields Cu-Mg$_{0.388}$Al$_{2.408}$O$_4$-BN a higher surface area (283.8 ± 3.7 m^2 g^{-1}) than that of Cu-Al$_2$O$_3$ (232.3 ± 2.9 m^2 g^{-1}). In addition, the BET surface area has a small decline with the addition of BN (Table S1) which may be attributed to the large size of BN (50–70 nm). The corresponding energy dispersive spectroscopy (EDS) taken from the cross-sectional SEM image confirms the existence of Cu, Mg, Al, O, B, and N elements in the catalyst
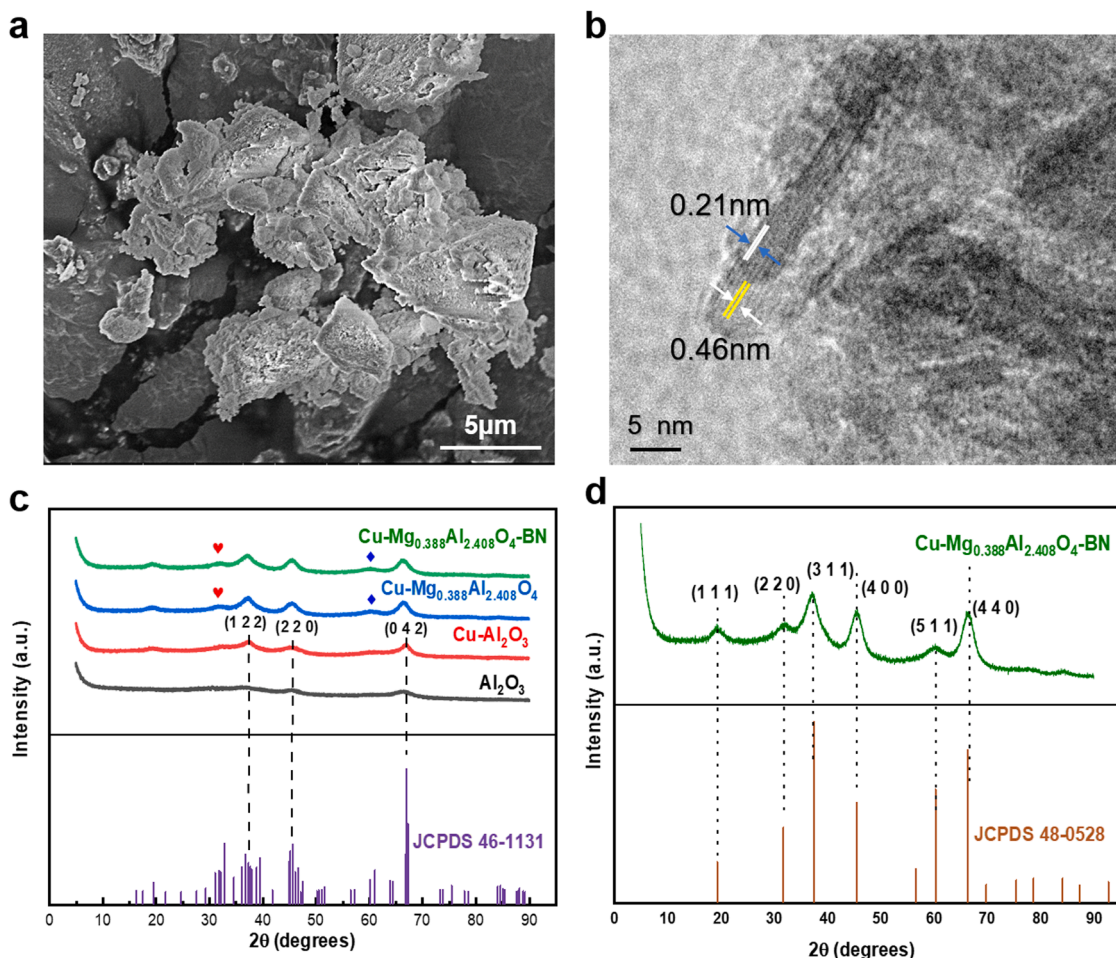
Fig. 1. (a) SEM of Cu-Mg$_{0.388}$Al$_{2.408}$O$_4$-BN; (b) TEM of Cu- Mg$_{0.388}$Al$_{2.408}$O$_4$-BN; (c) Wide angle XRD of different catalysts (black line is Al$_2$O$_3$, red line is Cu-Al$_2$O$_3$, blue line is Cu- Mg$_{0.388}$Al$_{2.408}$O$_4$, green line is Cu- Mg$_{0.388}$Al$_{2.408}$O$_4$-BN and the purple line is standard peaks of Al$_2$O$_3$); and (d) The comparison of XRD between Cu-Mg$_{0.388}$Al$_{2.408}$O$_4$-BN and standard peaks of Mg$_{0.388}$Al$_{2.408}$O$_4$ (green line is Cu- Mg$_{0.388}$Al$_{2.408}$O$_4$-BN and brown line is the standard peaks of Mg$_{0.388}$Al$_{2.408}$O$_4$).

(Fig. S1a). For example, the common metal Cu was uniformly dispersed (Fig. S1b) across the selected area. TEM image (Fig. 1b) also clearly shows the lattice fringe of the (111) plane of CuO and $Mg_{0.388}Al_{2.408}O_4$ with the interplanar spacing of 0.21 nm and 0.46 nm, respectively [34, 35], which indicated that Cu is embedded into the structure of $Mg_{0.388}Al_{2.408}O_4$. When Cu is doped into the lattice of $Mg_{0.388}Al_{2.408}O_4$, it will replace Al and connect with the lattice O to form CuO, leading to the lattice distortion on the surface [36]. In addition, as shown in Fig. S2a, pure BN showed an irregular morphology with the particle size of 50–70 nm in the TEM; the doped BN was also observed in the $Cu-Mg_{0.388}Al_{2.408}O_4$-BN composites as shown in Fig. S2b. The N_2 adsorption/desorption isotherms of $Cu-Mg_{0.388}Al_{2.408}O_4$-BN is in accordance with typical IV isotherms and the H3 hysteresis loop, which indicates the aggregation of slit-shaped pores and the mesopore (2–50 nm) structure for the catalysts (Fig. S3a). Then, the pore volume of the composite catalyst is 0.482 cm^3/g and the pore size is 7.238 nm (Fig. S3b).

The XRD patterns of prepared catalysts are shown in Fig. 1c. The pure Al_2O_3 appeared in the diffractogram with standard wide peaks which can be identified with JCPDS card No. 48 − 0528. There are three obvious peaks in Al_2O_3 spectra located at 37.3°, 45.6°, and 67.0°, which refer to the (1 2 2), (2 2 0), and (0 4 2) planes of Al_2O_3. After the insertion of copper, $Cu-Al_2O_3$ showed the same XRD pattern without the appearance of new diffraction peaks of Cu suggesting the absence of Cu nanoparticles and/or clusters formation. In addition, after doping of Mg, the XRD reflections for $Cu-Mg_{0.388}Al_{2.408}O_4$ and $Cu-Mg_{0.388}Al_{2.408}O_4$-BN are observed at 19.2°, 31.7°, 37.3°, 45.4°, 60.2°, and 66.3°, representing (1 1 1), (2 2 0), (3 1 1), (4 0 0), (5 1 1), and (4 4 0) planes of $Mg_{0.388}Al_{2.408}O_4$, which are well matched with the $Mg_{0.388}Al_{2.408}O_4$

crystal structure (JCPDS card No. 48 −0528) (Fig. 1d). Also, no peaks referred to Cu can be found in the diffractograms of $Cu-Mg_{0.388}Al_{2.408}O_4$ and $Cu-Mg_{0.388}Al_{2.408}O_4$-BN, further revealing that Cu may exist in the form of lattice doping coinciding with the TEM results. Based on the XRD data, we calculated the unit cell parameters (a, b, and c) for $Mg_{0.388}Al_{2.408}O_4$ and $Cu-Mg_{0.388}Al_{2.408}O_4$ (Table S2). It is found that the lattice parameters and unit cell volume increased in $Cu-Mg_{0.388}Al_{2.408}O_4$ compared with $Mg_{0.388}Al_{2.408}O_4$, which is attributed to the larger ionic radius of Cu(II) (0.073 nm) than Al(III) (0.053 nm) being replaced through the doping process [37]. In addition, the shape of peaks for $Cu-Mg_{0.388}Al_{2.408}O_4$-BN is almost the same as $Cu-Mg_{0.388}Al_{2.408}O_4$, which indicates BN did not alter the structure of the $Cu-Mg_{0.388}Al_{2.408}O_4$. Based on the weight of the final product (2.242 g) and BN addition (0.015 g), there is only about 0.67 wt% of BN in $Cu-Mg_{0.388}Al_{2.408}O_4$-BN.

Electrochemical impedance spectroscopy (EIS) was applied to analyze the electron transfer ability of different samples (Fig. 2a-c). From the enlarged image, it is observed that the Nyquist plot diameters of different samples are in the following order BN > $Cu-Al_2O_3$ > $Cu-Mg_{0.388}Al_{2.408}O_4$ > $Cu-Al_2O_3$-BN > $Cu-Mg_{0.388}Al_{2.408}O_4$-BN in the absence of PMS and BPA. A large diameter indicates poor conductivity which is not favorable for the electron transfer process. When PMS was involved in the reaction, the electron transmission rates of $Cu-Al_2O_3$-BN and $Cu-Mg_{0.388}Al_{2.408}O_4$-BN were greatly improved. The addition of BN can promote the cation-π effect which can enhance the polarization difference of the catalyst for effective PMS activation. Interestingly, when BPA was also involved in the reaction, $Cu-Mg_{0.388}Al_{2.408}O_4$-BN showed the best performance in the electron transfer process among all of the samples. This is because BPA as an electron donor may trigger the
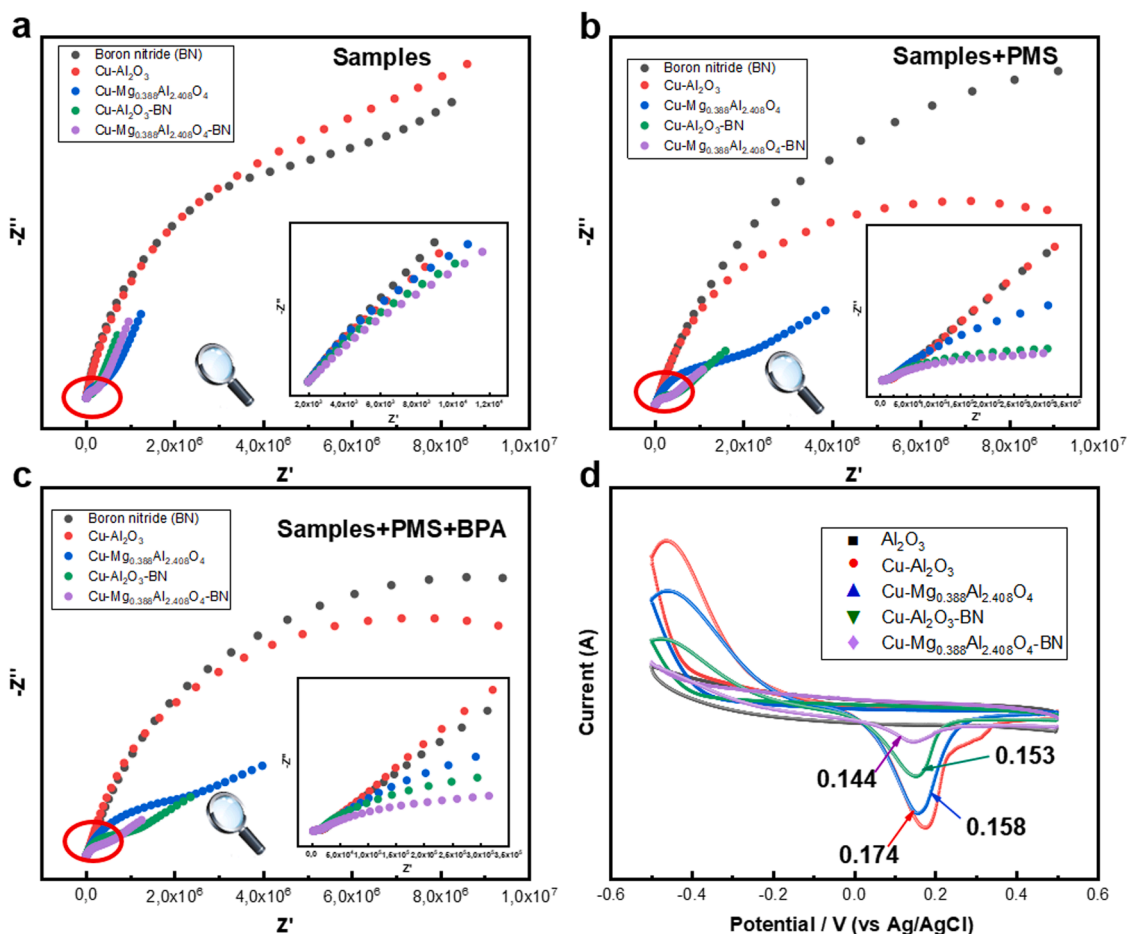

Fig. 2. (a-c) Electrochemical impedance spectroscopy (EIS) of different treated samples (Inserted plots are enlarged EIS); and (d) CV curve of different catalysts.

dual-reaction center to accelerate electron transfers and also can form π-π conjugation with BN to enhance electron transfer. In other words, Cu-Mg$_{0.388}$Al$_{2.408}$O$_4$-BN with the strongest polarization difference can transfer electrons quickly in the presence of electron-donor BPA. Fig. 2d shows the cyclic voltammetry (CV) data of different samples. No reduction peak can be observed for Al$_2$O$_3$, while the downward peaks of Cu(I)/Cu(II) reduction potential were observed for γ-Cu-Al$_2$O$_3$ (0.174 V), Cu-Mg$_{0.388}$Al$_{2.408}$O$_4$ (0.158 V), Cu-Al$_2$O$_3$-BN (0.153 V) and Cu-Mg$_{0.388}$Al$_{2.408}$O$_4$-BN (0.144 V) under the same conditions. Generally, the lower reduction potential means the weaker oxidation of metal elements in the sample. As we all know, Mg with low electronegativity can enhance the electron cloud density of Cu, and BN can also compensate electrons to Cu via the cation-π effect [38]. Therefore, Cu will become more and more difficult to obtain external electrons in the Cu-Mg$_{0.388}$Al$_{2.408}$O$_4$, Cu-Al$_2$O$_3$-BN and Cu-Mg$_{0.388}$Al$_{2.408}$O$_4$-BN.

X-ray photoelectron spectroscopy (XPS) was used to analyze the chemical states of elements on the catalyst surface. The B 1 s spectrum of BN can be deconvoluted into two peaks (Fig. S4a): i) one at 190.1 eV is ascribed to the B-N bond, and ii) another one centred at 192.5 eV is assigned to the B-O bond [39]. Based on the previous report, we can infer that the surface Cu can be linked to B in BN by σ bonding and to oxygen in the hydroxyl group to form a B-O-Cu cross-linker [40]. This inference can be proven by the blue shift of the ν(OH) in FTIR spectra of Cu-Mg$_{0.388}$Al$_{2.408}$O$_4$-BN (3409 cm^{-1}) compared with that of Cu-Mg$_{0.388}$Al$_{2.408}$O$_4$ (3415 cm^{-1}) [7] (Fig. S5). The O 1s profiles of Cu-Mg$_{0.388}$Al$_{2.408}$O$_4$-BN were deconvoluted into three oxygen species as shown in Fig. S4b. The peak at a binding energy of 530.2 eV can be assigned to O$_{lattice}$, coming from the lattice oxygen, the peak at 531.5 eV

is considered as chemisorbed-oxygen species (O$_{ads}$), and the strongest binding energy peak located at 532.5 eV is attributed to physically or chemically adsorbed H$_2$O$_{(O_{H_2O})}$ [41].

Fig. 3a demonstrates the high-resolution Cu 2p$_{3/2}$ for the Cu-modified samples. Each Cu 2p$_{3/2}$ spectrum for the Cu-Al$_2$O$_3$ sample is deconvoluted into three peaks, corresponding to the satellite peak at 942.1 eV, Cu^{2+} at 934.2 eV and Cu$^+$ at 932.5 eV (Fig. 3a) [17]. For Cu-Mg$_{0.388}$Al$_{2.408}$O$_4$ and Cu-Al$_2$O$_3$-BN, a small negative shift in the binding energy occurred on the peaks of Cu as compared to the Cu-Al$_2$O$_3$ sample (Fig. 3b-c). This can be explained by the relatively large electronegativity of Cu in Cu-Mg$_{0.388}$Al$_{2.408}$O$_4$ which causes the lone pair of electrons on Mg and Al to shift to Cu increasing the electron density around Cu [12]. On the other hand, BN can also transfer electrons to Cu through the action of cation-π. Therefore, the binding ability of the Cu nucleus to extranuclear electrons will be weakened, and the binding energy will be reduced, i.e., small blue shifts. Cu-Mg$_{0.388}$Al$_{2.408}$O$_4$-BN contains BN and Mg together, consequently showed the largest shift towards lower binding energy to 931.7 eV for Cu$^+$, 933.4 eV for Cu^{2+}, and 940.5 eV for the satellite peak (Fig. 3d), indicating the enhanced ability to transfer electrons. Furthermore, the ratio of Cu(I)/Cu(II) of catalysts was calculated by the area ratio of Cu(I) and Cu(II) in the XPS, which followed the order of Cu-Mg$_{0.388}$Al$_{2.408}$O$_4$-BN (1.31) > Cu-Al$_2$O$_3$-BN (0.93) > Cu-Mg$_{0.388}$Al$_{2.408}$O$_4$ (0.616) > Cu-Al$_2$O$_3$ (0.57). This result reveals that the content of Cu in the reduced state (Cu$^+$) gradually increases with the incorporation of Mg and BN into the catalysts, i.e., there are more electrons around Cu to keep it in a lower valence state. Therefore, the above results indicate the enrichment of electrons at the Cu sites in Cu-Mg$_{0.388}$Al$_{2.408}$O$_4$-BN.
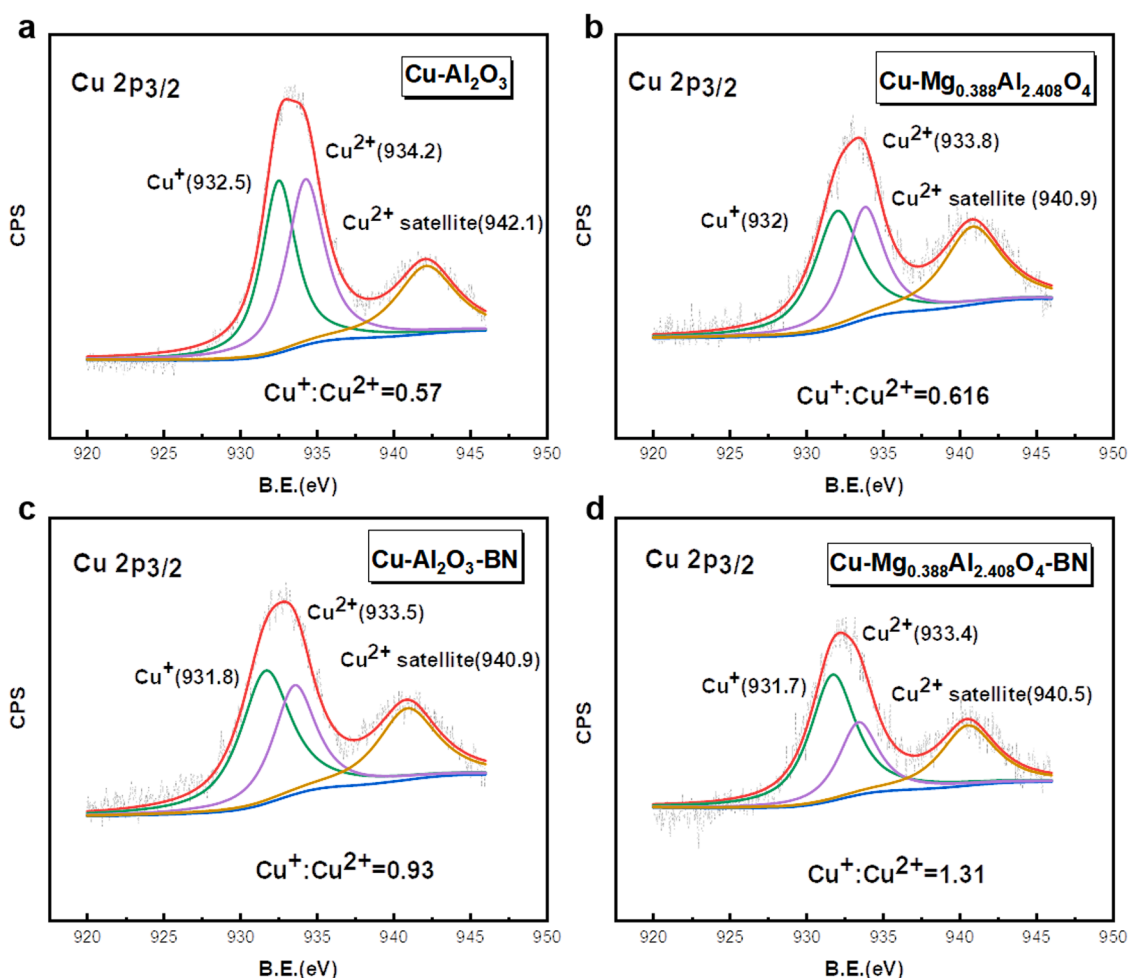

Fig. 3. Cu 2p3/2 peaks of (a) Cu-Al$_2$O$_3$, (b) Cu-Mg$_{0.388}$Al$_{2.408}$O$_4$, (c) Cu-Al$_2$O$_3$-BN, and (d) Cu-Mg$_{0.388}$Al$_{2.408}$O$_4$-BN in XPS spectra.

Fig. S6 shows the zeta potentials of the as-prepared catalyst particles at different pH values. The PZC of Cu-Al$_2$O$_3$ and Cu-Al$_2$O$_3$-BN are near 10. However, even if the pH of the solution reaches up to 11, Cu-Mg$_{0.388}$Al$_{2.408}$O$_4$-BN still does not reach the zero point of charge. Hence, the Cu-Mg$_{0.388}$Al$_{2.408}$O$_4$-BN surface is positive-charged in the tested pH range favorable for the adsorption of negatively charged PMS and BPA anions. Electrostatic adsorption plays a very important role in this system. As an electron donor, the adsorbed BPA can quickly transfer electrons to the surface of Cu-Mg$_{0.388}$Al$_{2.408}$O$_4$-BN provided with the synergistic effect of electrostatic attraction and dual-reaction center. At the same time, the accumulated PMS on the surface can also quickly trap the electrons near the electron-rich center to reduce themselves for generating SO$_4^{\bullet-}$ and then $^\bullet$OH.

3.2. Catalyst performance

BPA degradation experiments were conducted to show the abilities of different catalysts for PMS activation. The degradation kinetics of BPA is well fitted to the pseudo-first-order kinetic model, $-\ln(C/C_0) = kt$ ("C" is the concentration of BPA at different times, "C_0" is the initial concentration of BPA, "k" is the rate constant, and "t" is the reaction time), which agrees with previous BPA degradation studies [42,43]. Cu-Mg$_{0.388}$Al$_{2.408}$O$_4$-BN exhibited much higher catalytic activity compared with Cu-Al$_2$O$_3$ and Cu-Mg$_{0.388}$Al$_{2.408}$O$_4$ (Fig. 4a). More than 98% of BPA (20 mg L^{-1}) was degraded by Cu-Mg$_{0.388}$Al$_{2.408}$O$_4$-BN (1 g L^{-1}) within 45 min (PMS = 1 mM) and nearly 80% removal can be reached within the initial 4 min at which Cu-Al$_2$O$_3$ and

Cu-Mg$_{0.388}$Al$_{2.408}$O$_4$ only achieved 25% and 72% removal efficiencies, respectively. In addition, another two control samples without Cu (Mg$_{0.388}$Al$_{2.408}$O$_4$ and Mg$_{0.388}$Al$_{2.408}$O$_4$-BN) were prepared. As shown in Fig. S7a, both samples demonstrate very low degradation for BPA within 45 min (21%). It appears that dual-reaction center was not formed without Cu doping which leads to limited BPA degradation. Notably, Mg$_{0.388}$Al$_{2.408}$O$_4$-BN exhibited a better performance (21%) compared with Mg$_{0.388}$Al$_{2.408}$O$_4$ (6%) which may be attributed to the stronger polarization difference induced by BN on the Mg$_{0.388}$Al$_{2.408}$O$_4$-BN surface than that of Mg$_{0.388}$Al$_{2.408}$O$_4$. Although Mg$_{0.388}$Al$_{2.408}$O$_4$ and Mg$_{0.388}$Al$_{2.408}$O$_4$-BN have weak abilities for PMS activation, they exhibited very rapid PMS consumption as shown in Fig. S8, especially in the first 4 min. It indicated that Mg$_{0.388}$Al$_{2.408}$O$_4$ have a good adsorption ability for PMS. As mentioned above, Cu- Mg$_{0.388}$Al$_{2.408}$O$_4$-BN exhibit a rapid degradation for BPA at the first 4 min (Fig. 4a), which means massive SO$_4^{\bullet-}$ generation via PMS activation. Therefore, the accumulated PMS on the catalyst surface quickly trap the electrons near the electron-rich center to reduce themselves, yielding such rapid BPA degradation. As shown in Table S3, only 4.8% of BPA is adsorbed by Cu-Al$_2$O$_3$ while 15.2% of BPA could be adsorbed by Cu-Mg$_{0.388}$Al$_{2.408}$O$_4$-BN, indicating favorable BPA adsorption via electrostatic interaction. In the initial stage of the reaction (20 mg L^{-1} BPA and 1 mM PMS, respectively), rapid PMS adsorption and activation occurred on the surface of Cu-Mg$_{0.388}$Al$_{2.408}$O$_4$-BN, due to the electrostatic adsorption and the extremely strong polarization difference. At the same time, BPA can quickly be adsorbed on the catalyst surface and transfer electrons to the Cu center. Therefore, the adsorbed PMS quickly capture the
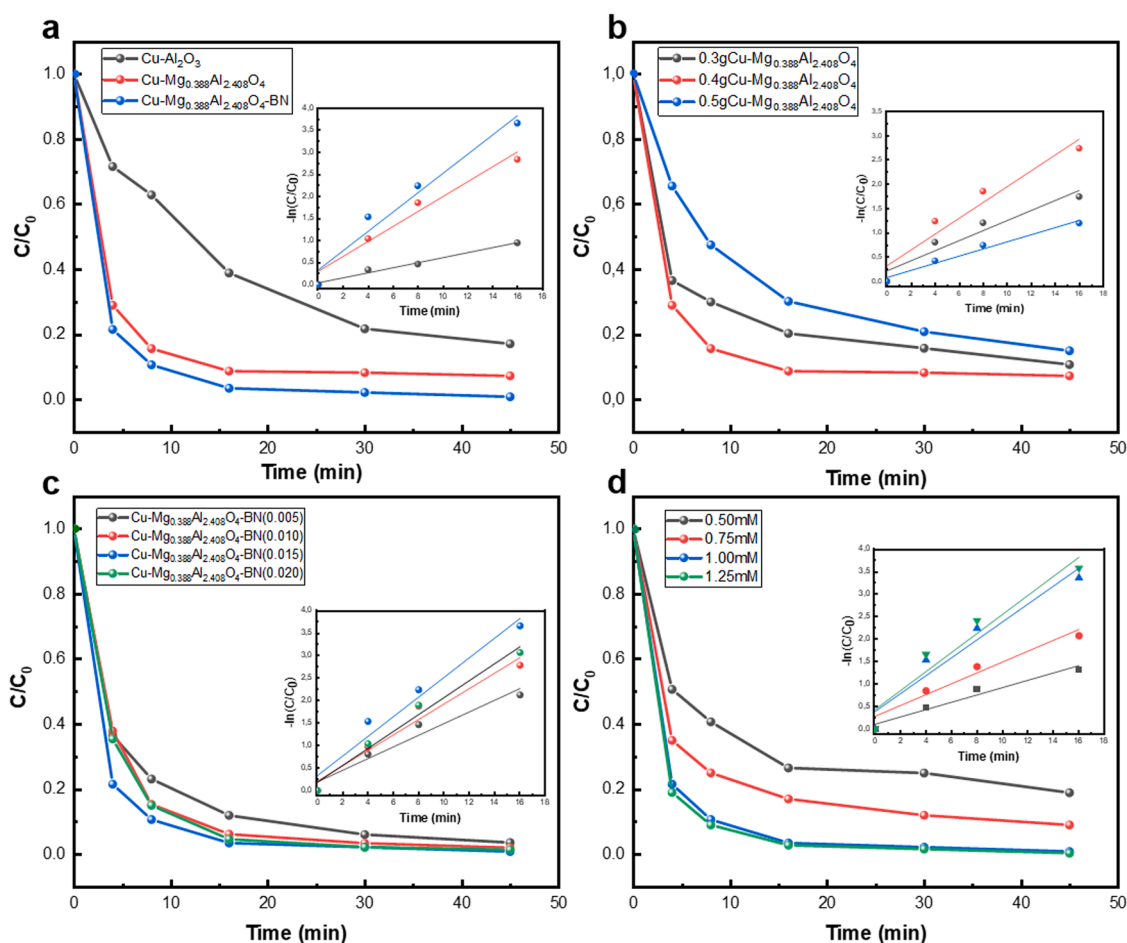

Fig. 4. (a) BPA degradation using various samples; (b) BPA degradation using Cu-Mg$_{0.388}$Al$_{2.408}$O$_4$ with different content of Cu; (c) BPA degradation over Cu-Mg$_{0.388}$Al$_{2.408}$O$_4$-BN with different content of BN [Initial PMS concentration = 1 mM, initial pH = 5.6, catalyst concentration = 1 g L^{-1}, BPA concentration = 20 mg L^{-1})]; (d) BPA degradation using Cu-Mg$_{0.388}$Al$_{2.408}$O$_4$ -BN at different concentration of PMS (the inserted plots are the fitted first-order kinetic curves).

electrons around Cu to generate $SO_4^{\bullet-}$ to degrade the adsorbed BPA. The degradation performance of Cu-Mg$_{0.388}$Al$_{2.408}$O$_4$-BN for 3 other pollutants including sulfamethoxazole (antibiotic), rhodamine B (dye), and acid orange 7 (dye) were also tested under the same conditions. From Fig. S9a, Cu-Mg$_{0.388}$Al$_{2.408}$O$_4$-BN can remove over 90% of these pollutants within 45 min, reaffirming its high PMS activation efficiency.

Next, the activities of Cu-Mg$_{0.388}$Al$_{2.408}$O$_4$ with different Cu contents (4.9, 6.3 and 7.3 wt%) were tested, following the order of 6.3 wt% (0.4CM) > 4.9 wt% (0.3CM) > 7.3 wt% (0.6CM) (Fig. 4b). Hence, 6.3 wt% Cu content was selected as the optimum doping amount. During the synthesis process, a proper amount of Cu can be doped into the framework of the Cu-Mg$_{0.388}$Al$_{2.408}$O$_4$, while an excessive amount of Cu addition will promote to form of the extra framework copper species such as CuO oxides or Cu nanoparticles which may inhibit the contact between PMS and internal copper species in the PMS activation reaction [44]. Thus, 7.3 wt% Cu-Mg$_{0.388}$Al$_{2.408}$O$_4$ exhibited lower catalytic activity than 6.3 wt% Cu-Mg$_{0.388}$Al$_{2.408}$O$_4$. In addition, as shown in Fig. 4c different BN loadings also affected the catalytic performance following the order of CM-0.015BN > CM-0.02BN > CM-0.01BN > CM-0.005BN. The added amount of 0.015BN seems to not only increase the polarity difference via the cation-π reaction, but also avoid coverage of reaction sites by BN. With poor conductivity itself, too much BN will hinder the electron transfer in the reaction.

Furthermore, the influence of PMS concentration on BPA degradation was also tested with 1 g L^{-1} catalyst dosage (Fig. 4d). More than 98% BPA was removed when 1 mM PMS was added into Cu-Mg$_{0.388}$Al$_{2.408}$O$_4$-BN suspension within 45 min. When the concentration of PMS decreased to 0.5 mM, about 80% BPA was removed. However, there is no obvious increase in the degradation efficiency of BPA at PMS concentration up to 1.25 mM. Although the adsorbed PMS can be decomposed rapidly to form $SO_4^{\bullet-}$ and $^{\bullet}OH$ for BPA degradation, excess PMS does not promote the degradation efficiency of BPA due to its radical scavenging effect. Therefore, 1 mM PMS addition was considered as the optimal concentration employed in this study.

Since real wastewater usually contains various co-existing anions including chloride ion (Cl$^-$), sulfate ion (SO_4^{2-}), nitrate ion (NO$_3^-$) and dihydrogen phosphate ion (H$_2$PO$_4^-$), their impacts on BPA degradation experiments were analyzed. As shown in Fig. S9b, their inhibition effects on BPA degradation were in the order of H$_2$PO$_4^-$ > SO$_4^{2-}$ > NO$_3^-$ > Cl$^-$. It is reported that Cl$^-$ can react with $^{\bullet}OH$ and $SO_4^{\bullet-}$ to produce $^{\bullet}ClO$ and $^{\bullet}Cl$ radicals that still degrade BPA [45]. However, NO$_3^-$ can react with $^{\bullet}OH$ and $SO_4^{\bullet-}$ to form nitrate radicals which is much less reactive, resulting in reduced BPA degradation [46]. Similarly, H$_2$PO$_4^-$ could scavenge $^{\bullet}OH$ and $SO_4^{\bullet-}$ inhabiting the degradation reaction too [47]. As comparison,

the inhibition of the degradation process by SO_4^{2-} was probably due to the fact that SO_4^{2-} with more negative charges could be easily attracted by the positive-charged surface of Cu-Mg$_{0.388}$Al$_{2.408}$O$_4$-BN and cover the reaction sites resulting in decreased reaction rates [48].

Notably, Cu-Mg$_{0.388}$Al$_{2.408}$O$_4$-BN achieved near 40% TOC removal rate within 45 min, which is much higher than that of Cu-Al$_2$O$_3$ (about 7%) (Fig. 5a). Furthermore, we used the ratio of ΔTOC / ΔPMS to evaluate the utilization of PMS (η) in the system (Fig. 5a). In the initial 8 min, PMS has a good utilization efficiency in both systems. This result can be explained by the higher concentrations of both PMS and pollutants in the initial stage, thus the catalyst can activate PMS to produce sufficient radicals to mineralize BPA. In particular, the PMS utilization efficiency of Cu-Mg$_{0.388}$Al$_{2.408}$O$_4$-BN in the initial stage is almost four times greater than that of Cu-Al$_2$O$_3$. The adsorption of PMS and BPA on the positive-charged surface not only makes PMS decompose more effectively, but also reduces the migration distance of $SO_4^{\bullet-}$ and $^{\bullet}OH$ to retain the activity. On the other hand, we can see that the utilization efficiency of both Cu-Mg$_{0.388}$Al$_{2.408}$O$_4$-BN and Cu-Al$_2$O$_3$ for PMS decreased over time, but the declining rate of Cu-Al$_2$O$_3$ is significantly faster than that of Cu-Mg$_{0.388}$Al$_{2.408}$O$_4$-BN. With the dual-reaction center effect, the activity of catalytic sites on Cu-Mg$_{0.388}$Al$_{2.408}$O$_4$-BN is more stable and thus maintains a higher utilization rate of PMS in the later reaction stage. However, for Cu-Al$_2$O$_3$, high valent Cu(II) accumulates in the later stage, resulting in rapidly decreased activity and the low utilization rate of PMS.

The leaching amount of Cu from Cu-Mg$_{0.388}$Al$_{2.408}$O$_4$-BN (0.13 mg L^{-1}) is significantly low, only accounting for 0.2% of the total Cu in the system (Fig. S10); no leaching of Al and Mg was observed during the degradation process either. Moreover, the degradation efficiency of BPA over Cu-Mg$_{0.388}$Al$_{2.408}$O$_4$-BN can remain more than 97% within 45 min after 4 successive cycles (Fig. 5b). The kinetic reaction rate decline after the first use but remain to be moderate even after four reusability experiments (Fig. S7b). Likewise, the SEM and XRD results demonstrate no obvious change in the catalyst after the reaction (Fig. S11). The improvement of stability for Cu-Mg$_{0.388}$Al$_{2.408}$O$_4$-BN could be explained by two reasons: (1) the dual-reaction center can avoid the redox cycle of Cu and any wasteful use of PMS, and (2) the structure of Mg$_{0.388}$Al$_{2.408}$O$_4$ is shown to be stable as evidenced by the leaching results.

3.3. Catalytic mechanism

The valence electron density analysis was performed for the constructed model of Cu-Mg$_{0.388}$Al$_{2.408}$O$_4$-BN, in which the transparent
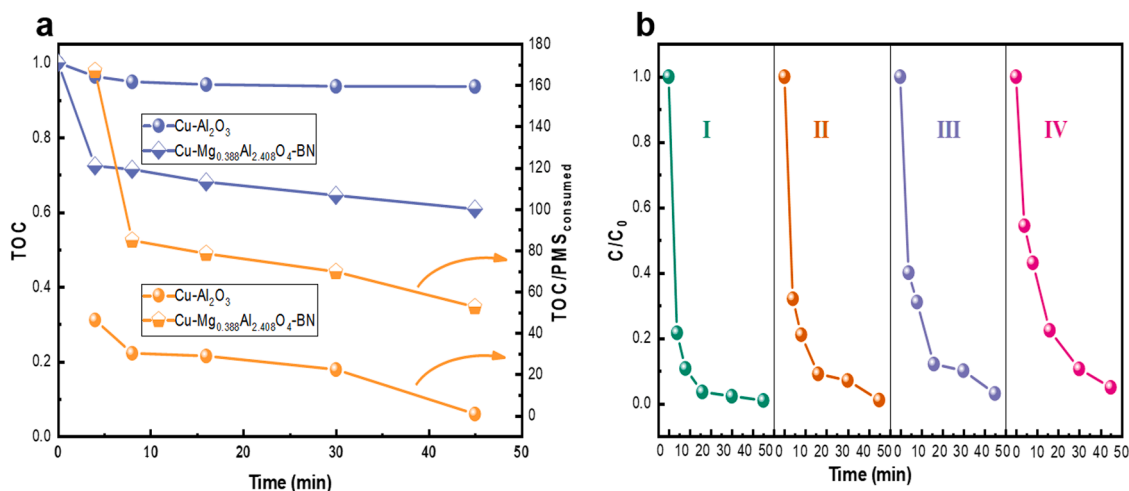

Fig. 5. (a) TOC removal and utilization efficiency of PMS over Cu-Al$_2$O$_3$ and Cu-Mg$_{0.388}$Al$_{2.408}$O$_4$-BN in the process of BPA degradation. (b) Reusability of Cu-Mg$_{0.388}$Al$_{2.408}$O$_4$-BN for BPA degradation (catalyst concentration = 1 g L^{-1}, PMS concentration = 1 mM, initial pH = 5.6, initial BPA concentration = 20 mg L^{-1}).

isosurface on the elements represents electron-rich regions, while those without are electron-poor regions (Fig. 6a). The valence electron cloud density of surrounding Cu is high as an electron-rich region, while the naked Al and Mg atoms demonstrate to be electron-deficient centers due to their low electronegativity. In addition, B elements in BN also become electron-deficient due to the electron transfer to Cu via the cation-π interaction. The DFT calculation results indicate that a polarization difference has been induced on this dual-reaction center catalyst. However, whether this polarization difference is so strong to well-separated redox reaction sites to form a dual-reaction center and reduce the occurrence of rate-limiting steps requires further verification. In addition, the adsorption energy can be used to compare the adsorption abilities of catalysts for the reactants. As shown in Fig. 6b and d, the adsorption energy of Cu-$Mg_{0.388}Al_{2.408}O_4$-BN for PMS and is −1.067 eV which is more negative than that of Cu-Al_2O_3-BN (−0.923 eV), which means Mg can promote the adsorption for PMS. Moreover, Mg can connect with O atom of PMS to form a bond with a bond length of 2.136 Å, which also proves the strong adsorption ability of $Mg_{0.388}Al_{2.408}O_4$ for PMS and provides the possibility of electron transfer between catalyst and PMS. (Fig. 6b). Also, the negative adsorption energy between Cu-$Mg_{0.388}Al_{2.408}O_4$-BN and BPA (−2.165 eV) indicated BPA can adsorb on the surface of Cu-$Mg_{0.388}Al_{2.408}O_4$-BN for subsequent degradation (Fig. 6c).

To verify the formation of dual-reaction center in our catalysts, we performed the XPS analysis of Cu after the catalytic reactions for Cu-Al_2O_3, Cu-$Mg_{0.388}Al_{2.408}O_4$, Cu-Al_2O_3-BN, and Cu-$Mg_{0.388}Al_{2.408}O_4$-BN. The ratio of Cu(I)/Cu(II) of Cu-Al_2O_3 showed the largest drop from 0.57 to 0.43 after the reaction (Fig. 7a). In contrast, the Cu(I)/Cu(II) ratio decreased moderately from 0.62 to 0.50 and from 0.93 to 0.84 for Cu-$Mg_{0.388}Al_{2.408}O_4$ and Cu-Al_2O_3-BN (Fig. 7b-c), respectively. The relatively higher content of Cu(I) in Cu-$Mg_{0.388}Al_{2.408}O_4$ and Cu-Al_2O_3-BN is due to the low-electronegativity of Mg compared to Cu and the cation-π effect between Cu and BN, respectively. However, their ratio drops are

still noticeable without producing an obvious dual-reaction center on the catalyst surface. As we anticipated, the smallest change of the Cu(I)/Cu(II) ratio occurred in the Cu-$Mg_{0.388}Al_{2.408}O_4$-BN system (Fig. 7d), i. e., the value insignificantly decreased from 1.31 to 1.28. This negligible change is due to the strongest electron-rich Cu center formation in Cu-$Mg_{0.388}Al_{2.408}O_4$-BN. These results reflect the fact that using a dual-reaction center can potentially replace the use of transition metals, which usually work as active centers on the catalyst surface for redox reactions. Through dual-reaction center design, the redox cycle of Cu(I)/Cu(II) is avoided and any wasteful decomposition of PMS caused by the reduction of Cu(II) is also reduced.

In order to prove the improved PMS decomposition ability, we measured the residual concentration of PMS in the reaction solution using the KI method at different reaction times. As depicted in Fig. 8, Cu-$Mg_{0.388}Al_{2.408}O_4$-BN showed a much faster decomposition rate of PMS than Cu-Al_2O_3, i.e., 42.6% PMS was consumed by Cu-$Mg_{0.388}Al_{2.408}O_4$-BN within 45 min and nearly 19.7% of consumption occurred in the initial 4 min. In comparison, only 18.0% and 1.3% PMS were consumed within 45 min and 4 min, respectively, for Cu-Al_2O_3. This could be due to the flowing reasons: i) HSO_5^- adsorbed on the surface of Cu-$Mg_{0.388}Al_{2.408}O_4$-BN quickly via electrostatic attraction and decomposed into $SO_4^{\bullet-}$, and ii) there are more Cu(I) in the catalyst of Cu-$Mg_{0.388}Al_{2.408}O_4$-BN compared of Cu-Al_2O_3, so it is more likely that PMS was reduced by the surface Cu(I) through its redox cycle in this system. Therefore, PMS was consumed more rapidly in the system of Cu-$Mg_{0.388}Al_{2.408}O_4$-BN.

Interestingly, the decompositions of PMS in both systems were enhanced in the presence of BPA. The phenolic OH group and surface Cu (II) can form σ-Cu ligand, which facilitates the reduction of Cu(II) to Cu (I). That is why there is an obvious increase in PMS consumption in the system of Cu-Al_2O_3 with the addition of BPA. In the system of Cu-$Mg_{0.388}Al_{2.408}O_4$-BN, BPA also acts as an excellent electron donor to the electron-poor areas (Mg, Al, and BN) via electrostatic adsorption and π-π
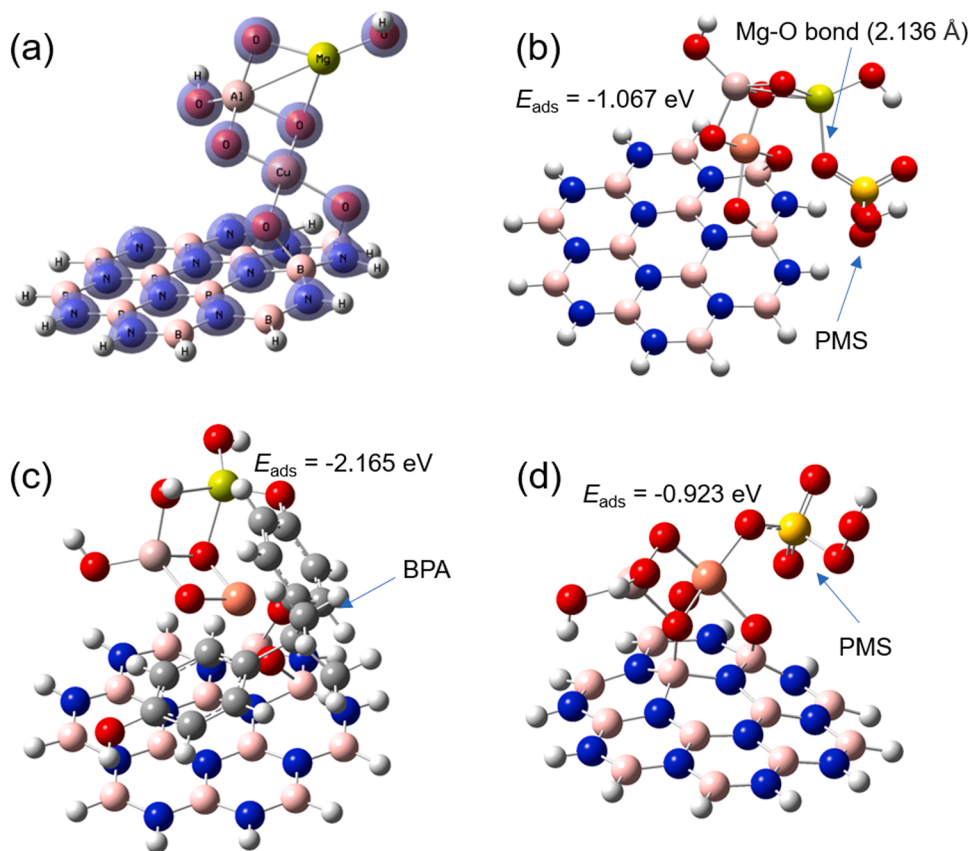

Fig. 6. (a) The valence electron density of BN growing on the surface of Cu doped $Mg_{0.388}Al_{2.408}O_4$ through the connection of B-O-Cu drawn based on DFT calculation using Gaussian 16 A.03 program at B3LYP-D3/6–31 G(d) level (This simplified structure can be considered as a unit of the whole structure of dual-reaction center). (b) Optimized configuration of PMS adsorbed on Cu-$Mg_{0.388}Al_{2.408}O_4$-BN. (c) Optimized configuration of BPA adsorbed on Cu-$Mg_{0.388}Al_{2.408}O_4$-BN. (d) Optimized configuration of PMS adsorbed on Cu-Al_2O_3-BN.
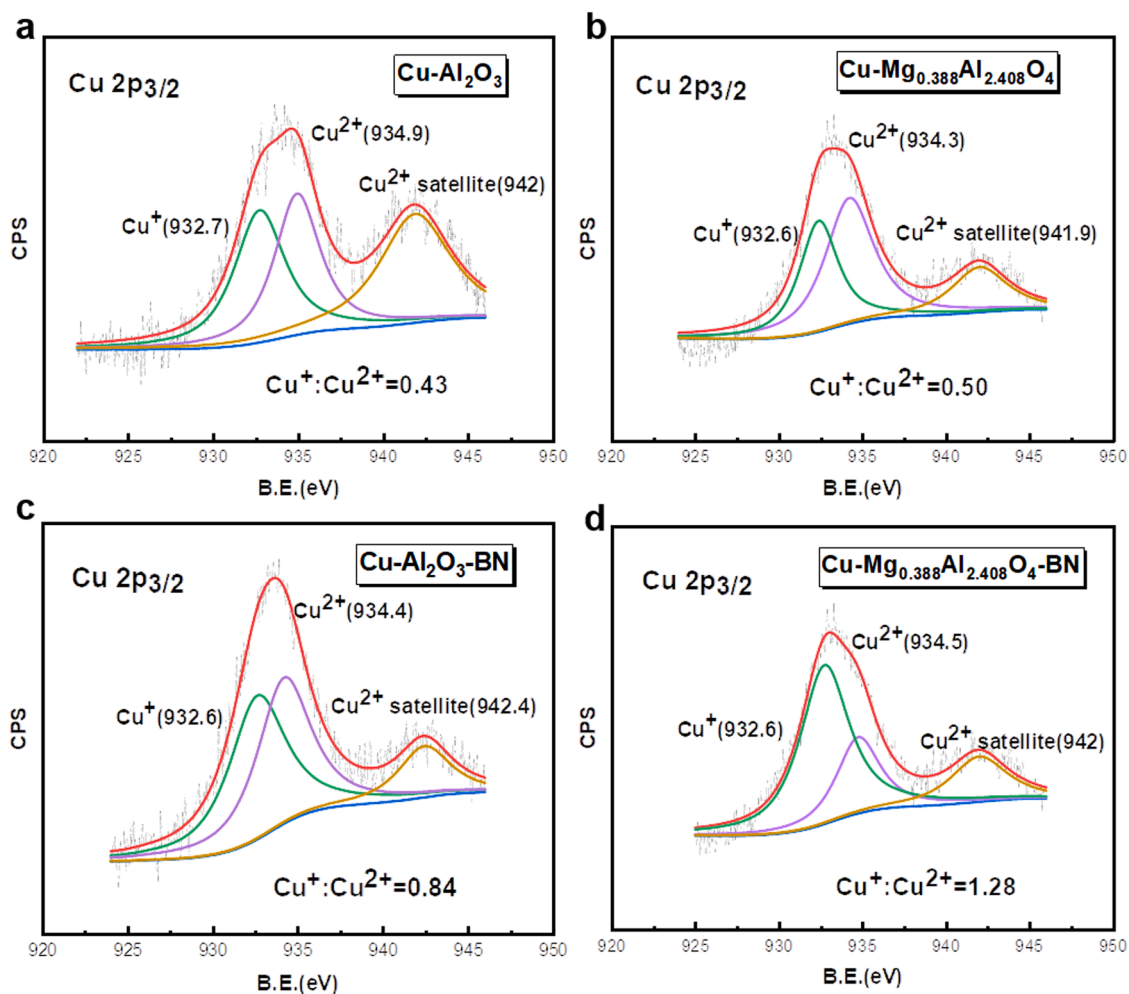
Fig. 7. Cu 2p3/2 peak in XPS spectra of (a) Cu-Al$_2$O$_3$, (b) Cu-Mg$_{0.388}$Al$_{2.408}$O$_4$, (c) Cu-Al$_2$O$_3$-BN and (d) Cu-Mg$_{0.388}$Al$_{2.408}$O$_4$-BN after the reaction.

conjugation effect. After the electrons are transferred to the Cu center, the adsorbed PMS can capture these electrons for self-reduction to generate SO$_4^{\bullet-}$ that can attack the BPA and its intermediate products adsorbed on the catalyst surface. Following degradation, the adsorption sites can be released for BPA adsorption again, thereby repeating the electron transfer path on the catalyst surface in the next cyclic reactions.

Fig. 8. PMS consumption in the system of Cu-Al$_2$O$_3$, Cu-Al$_2$O$_3$ + BPA, Cu-Mg$_{0.388}$Al$_{2.408}$O$_4$-BN and Cu-Mg$_{0.388}$Al$_{2.408}$O$_4$-BN + BPA (The numbers in the figures refer to absorbance).
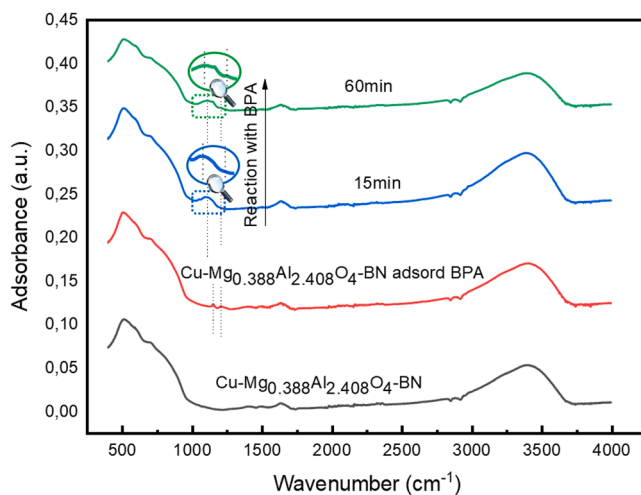

Fig. 9. FT-IR spectra for Cu-Mg$_{0.388}$Al$_{2.408}$O$_4$-BN under different conditions (Inserted pictures are partially enlarged images of circled locations).

FTIR spectra of Cu-Mg$_{0.388}$Al$_{2.408}$O$_4$-BN were collected at different reaction stages and used to analyze the surface reaction processes (Fig. 9). The peaks located at 3406.9 and 1630 cm^{-1} of fresh Cu-Mg$_{0.388}$Al$_{2.408}$O$_4$-BN refer to OH [ν(OH)] stretching vibration and H-O-H bending vibration, respectively [49]. After the adsorption of BPA, new peaks at 1152 and 1210 cm^{-1} appeared which are corresponding to C−O stretching vibrations of the phenolic OH group of the BPA [50,51]. After 15 min reaction, a brand new peak located at 1103 cm^{-1} appeared. This peak is attributed to SO$_4^{2-}$ which comes from PMS decomposition [52]. Notably, after 1 h reaction, another new peak assigned to HSO$_5^-$ appeared at 1217 cm^{-1} [52]. These results indicated that PMS can be effectively converted to SO$_4^{\bullet-}$ at the initial stage of the reaction due to the high concentration of BPA available that donate electrons to PMS via the due-reaction center. These radicals can break down BPA and its transformation products (R$'$) to generate other products and SO$_4^{2-}$ (R + SO$_4^{\bullet-}$ → R$'$ + SO$_4^{2-}$ + H$^+$) which are adsorbed on the surface of Cu-Mg$_{0.388}$Al$_{2.408}$O$_4$-BN due to electrostatic attraction. While the concentrations of BPA and its immediate products decrease with reaction time, the rate of electron transfer also decreases. Until there are not enough electron donors supporting the reaction chain, some HSO$_5^-$ residuals accumulate on the catalyst surface.

The quenching experiments were conducted to identify the dominant reactive species during the BPA degradation. MeOH (with α-hydrogen) is regarded as an effective quencher for both $^\bullet$OH and SO$_4^{\bullet-}$ [53]. In contrast, TBA (without α-hydrogen) was used to selectively scavenge $^\bullet$OH due to its 1000 times greater rate constant ($k = 3.8 \times 10^8$ to 7.6×10^8 M^{-1} s^{-1}) than SO$_4^{\bullet-}$ ($k = 4.0 \times 10^5$ to 9.1×10^5 M^{-1} s^{-1}) [54]. Chloroform (CHCl$_3$) can work as an O$_2^{\bullet-}$ scavenger, provided its higher reaction rate constant with O$_2^{\bullet-}$ ($k = 3 \times 10^{10}$ M^{-1} s^{-1}) than with $^\bullet$OH ($k = 5 \times 10^6$ M^{-1} s^{-1}) [55]. Furfuryl alcohol (FFA) is an effective scavenger for ^{1}O$_2$ (1.2×10^8 M^{-1} s^{-1}), but can also quench $^\bullet$OH rapidly (1.5×10^{10} M^{-1} s^{-1}) [46]. The used concentrations of these reagents (methanol concentration = 100 mM, TBA concentration = 100 mM, chloroform concentration = 0.1 mM, FFA concentration = 15 mM) were to ensure complete scavenging of these radicals. As shown in Fig. 10, BPA was completely degraded within 45 min when no quenching agent was added. However, the removal of BPA declined to 66% in 30 min in the presence of TBA. Meanwhile, the addition of MeOH exhibited greater inhibition (52%) for the degradation of BPA. These results suggested that both SO$_4^{\bullet-}$ and $^\bullet$OH are the main active species for BPA

degradation in the Cu-Mg$_{0.388}$Al$_{2.408}$O$_4$−BN–PMS system. Notably, O$_2^{\bullet-}$ plays a small but non-negligible role in this process, evidenced by the slightly changed BPA degradation efficiency. Although there is an obvious drop in degradation after adding FFA in the system, the inhibition from FFA is very minor after subtracting the contribution from $^\bullet$OH, which means ^{1}O$_2$ is not the main ROS in this system.

In order to directly verify the radicals, EPR signals were collected using DMPO as a capture agent in different reaction systems. Interestingly, characteristic peaks of DMPO-$^\bullet$OH can be observed in Cu-Mg$_{0.388}$Al$_{2.408}$O$_4$−BN aqueous solution in the absence of PMS, which cannot be found in the Cu-Al$_2$O$_3$ aqueous solution (Fig. 11a). A strong polarization difference has been formed on the surface of Cu-Mg$_{0.388}$Al$_{2.408}$O$_4$−BN where H$_2$O as an electron donor can lose one electron to produce $^\bullet$OH in the electron-poor center. This result can also reflect the formation of a dual-reaction center in Cu-Mg$_{0.388}$Al$_{2.408}$O$_4$−BN. When PMS was added in the suspension of Cu-Al$_2$O$_3$ and Cu-Mg$_{0.388}$Al$_{2.408}$O$_4$−BN, the signals of DMPO-$^\bullet$OH were captured in both systems and the latter system had higher EPR intensities as shown in the Fig. 11b. Notably, we cannot find any peaks referred to SO$_4^{\bullet-}$, which is ascribed to the high reaction rate between DMPO and $^\bullet$OH (3.4×10^9 M^{-1} s^{-1}) [56] and the rapid conversion of DMPO-SO$_4^{\bullet-}$ to DMPO-$^\bullet$OH via a nucleophilic substitution [57]. With the participation of BPA in the system of Cu-Mg$_{0.388}$Al$_{2.408}$O$_4$-BN, there is a significant improvement of $^\bullet$OH generation, evidenced by the much higher EPR intensity (Fig. 11c and d). The addition of BPA as the electron donor has initiated the dual-reaction centers and transferred more electrons for PMS reduction to generate more free radicals than in the case of traditional PMS systems. Accordingly, the Cu-Mg$_{0.388}$Al$_{2.408}$O$_4$-BN system showed a much better PMS activation and degradation efficiency for BPA due to the synergistic effect between the dual-reaction center and electrostatic adsorption.

In light of the achieved results, the possible catalytic mechanism is proposed in Fig. 12. In the first step, Cu-Mg$_{0.388}$Al$_{2.408}$O$_4$-BN with a strong positive-charge surface could rapidly attract and enrich negatively charged BPA and PMS on the catalyst surface. Then, the dual-reaction center can work as an electron bridge for the transfer of electrons from BPA to PMS due to the large polarity difference. In detail, BPA provides electrons to the electron-poor center, which refers to Mg, Al, and BN sites then the donated electrons are transferred to Cu electron-rich center due to the polarity difference. Likewise, PMS adsorbed on the surface and captures these electrons at the Cu center to generate radicals for BPA degradation.

Based on the previous reports [58–62], we propose the potential degradation pathway of BPA by radicals in our dual-reaction center system. There are three different routes which were widely discussed on BPA degradation by radicals. As concluded in Fig. S12, SO$_4^{\bullet-}$ and $^\bullet$OH produced in the system might first attack the C—C bond between isopropyl and benzene rings via β-scission (Route 1) [63,64]. The produced phenol and 2-(4-hydroxyphenyl)-propanol-2-ol were further oxidized to form other intermediates with lower molecular weight. In addition, $^\bullet$OH can easily attack the benzene ring of BPA because of its electrophilic properties to form hydroxylated products (Route 2) [65,66] that will be further mineralized by undergoing a series of reactions including hydroxylation, dehydration, and molecular rearrangement. Moreover, some intermediates may react with BPA via H-abstraction and coupling reactions (Route 3) [67,68]. These molecules will be then decomposed via the β-scission similar to Route 1. In the end, the produced aromatic byproducts will be further transformed by ring-opening reactions and finally be oxidized into CO$_2$ and H$_2$O.

Fig. 10. Radical quenching tests of Cu-Mg$_{0.388}$Al$_{2.408}$O$_4$-BN (Condition: methanol concentration = 100 mM, TBA concentration = 100 mM, chloroform concentration = 0.1 mM, FFA concentration = 15 mM, catalyst concentration = 1 g L^{-1}, PMS concentration = 1 mM, initial pH = 5.6, initial BPA concentration = 20 mg L^{-1}).

4. Conclusion

A novel catalyst based on common metals, Cu-Mg$_{0.388}$Al$_{2.408}$O$_4$-BN with the dual-reaction center, was constructed and tested for PMS activation. The cation-π bond between Cu and BN promoted electron-rich Cu center formation which supplied electrons to PMS producing
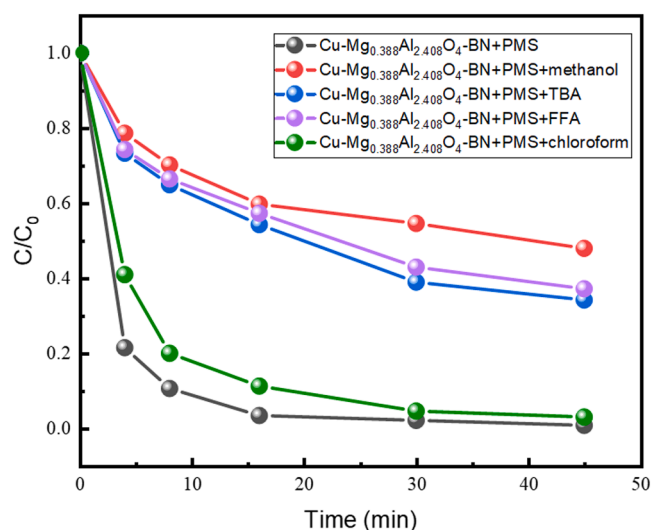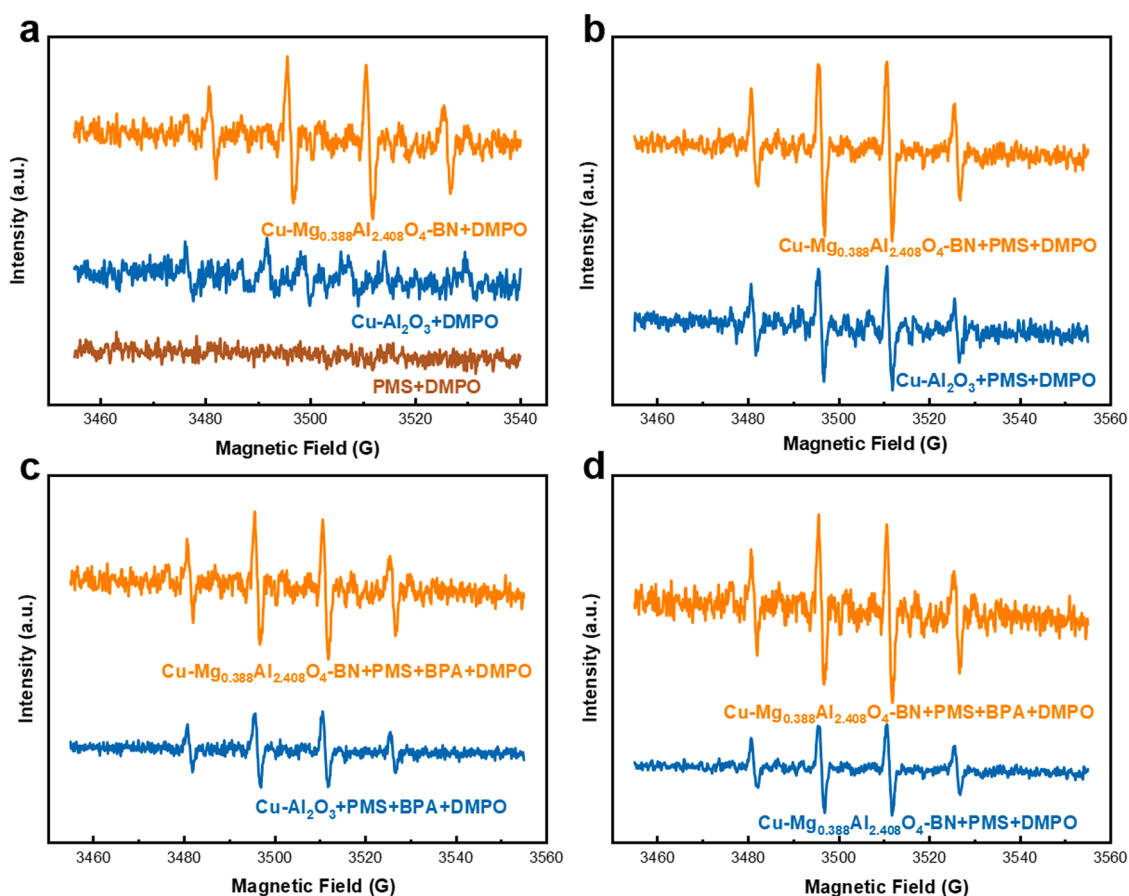
Fig. 11. EPR for (a) $^\bullet$OH in different aqueous dispersions without PMS; (b) $^\bullet$OH and $SO_4^{\bullet-}$ in various aqueous dispersions with PMS; (c) $^\bullet$OH and $SO_4^{\bullet-}$ in Cu-$Mg_{0.388}Al_{2.408}O_4$-BN suspensions in the presence of PMS with and without BPA; (d) $^\bullet$OH and $SO_4^{\bullet-}$ in various aqueous dispersions with PMS and BPA. (Condition: catalyst concentration = 1 g L^{-1}, PMS concentration = 1 mM, initial pH = 5.6, BPA concentration = 20 mg L^{-1} and DMPO concentration = 5 mM).
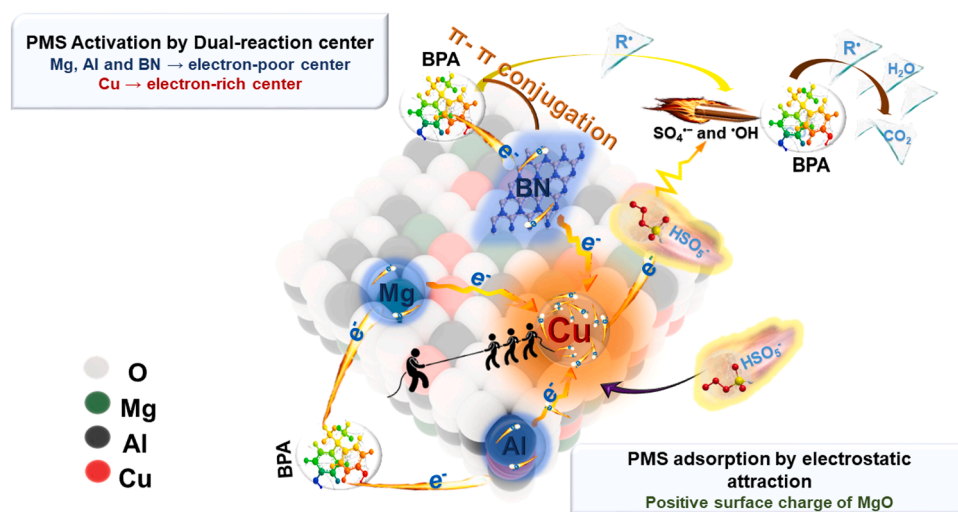

Fig. 12. Scheme of the possible degradation mechanism for BPA in PMS activation process using Cu-$Mg_{0.388}Al_{2.408}O_4$-BN.

$SO_4^{\bullet-}$ and $^\bullet$OH. In addition, BN enhanced the electron transfer from BPA to the electron-rich Cu center by the π-π effect, which endorsed the reduction of Cu(II) to Cu(I). Notably, $Mg_{0.388}Al_{2.408}O_4$-BN not only provided a very positive-charge surface for PMS and BPA adsorption, but also promoted the formation of electron-rich Cu center due to the large electronegativity difference between Cu and Mg/Al. The tailored dual-reaction center catalyst has achieved high PMS utilization and BPA mineralization. This synergistic effect between the dual-reaction center and adsorption mechanism provides a robust strategy for the design of efficient catalysts with low-cost metals and expands the application of Fenton-like processes in wastewater treatment. As compared with traditional Fenton-like systems based on expensive rare metal catalysts, this strategy is more economical and environmentally friendly. Before practical applications, potential interferences from the real water

matrix, loading of the catalyst onto suitable supporters, and adequate engineering designs should be carefully studied.

CRediT authorship contribution statement

Zhiqun Xie: Conceptualization, Methodology, Writing – original draft. **Dionysios D. Dionysiou:** Supervision, Writing – review & editing. **Shuang Luo:** Investigation, Validation. **Menglin Chen:** Resources, Writing – review & editing. **Zongsu Wei:** Conceptualization, Supervision, Writing – review & editing, Funding acquisition.

Declaration of Competing Interest

The authors declare that they have no known competing financial interests or personal relationships that could have appeared to influence the work reported in this paper.

Data Availability

Data will be made available on request.

Acknowledgements

Appendix A. Supporting information

Supplementary data associated with this article can be found in the online version at doi:10.1016/j.apcatb.2023.122468.

References

[1] L. Zhang, D. Xu, C. Hu, Y. Shi, Framework Cu-doped AlPO$_4$ as an effective Fenton-like catalyst for bisphenol A degradation, Appl. Catal. B: Environ. 207 (2017) 9–16.

[2] E. Saputra, S. Muhammad, H. Sun, H.-M. Ang, M.O. Tadé, S. Wang, Manganese oxides at different oxidation states for heterogeneous activation of peroxymonosulfate for phenol degradation in aqueous solutions, Appl. Catal. B: Environ. 142–143 (2013) 729–735.

[3] Z. Lyu, M. Xu, J. Wang, A. Li, P. François-Xavier Corvini, Hierarchical nano-vesicles with bimetal-encapsulated for peroxymonosulfate activation: singlet oxygen-dominated oxidation process, Chem. Eng. J. 433 (2022), 133581.

[4] X. Li, X. Huang, S. Xi, S. Miao, J. Ding, W. Cai, S. Liu, X. Yang, H. Yang, J. Gao, J. Wang, Y. Huang, T. Zhang, B. Liu, Single cobalt atoms anchored on porous N-doped graphene with dual reaction sites for efficient fenton-like catalysis, J. Am. Chem. Soc. 140 (2018) 12469–12475.

[5] W. Ma, N. Wang, Y. Du, T. Tong, L. Zhang, K.-Y. Andrew Lin, X. Han, One-step synthesis of novel Fe$_3$C@nitrogen-doped carbon nanotubes/graphene nanosheets for catalytic degradation of Bisphenol A in the presence of peroxymonosulfate, Chem. Eng. J. 356 (2019) 1022–1031.

[6] Z. Wen, Q. Zhu, J. Zhou, S. Zhao, J. Wang, A. Li, L. Chen, W. Bian, Flower-Shaped C-Dots/Co$_3$O$_4${111} constructed with dual-reaction centers for enhancement of fenton-like reaction activity and peroxymonosulfate conversion to sulfate radical, Catalysts 11.1 (2021) 135.

[7] S. Xu, H. Zhu, W. Cao, Z. Wen, J. Wang, C.P. François-Xavier, T. Wintgens, Cu-Al$_2$O$_3$-g-C$_3$N$_4$ and Cu-Al$_2$O$_3$-C-dots with dual-reaction centres for simultaneous enhancement of Fenton-like catalytic activity and selective H$_2$O$_2$ conversion to hydroxyl radicals, Appl. Catal. B: Environ. 234 (2018) 223–233.

[8] L. Lyu, G. Yu, L. Zhang, C. Hu, Y. Sun, 4-phenoxyphenol-functionalized reduced graphene oxide nanosheets: a metal-free fenton-like catalyst for pollutant destruction, Environ. Sci. Technol. 52 (2018) 747–756.

[9] J. Ma, L. Xu, C. Shen, C. Hu, W. Liu, Y. Wen, Fe-N-Graphene wrapped Al$_2$O$_3$/pentlandite from microalgae: high fenton catalytic efficiency from enhanced Fe(3 +) reduction, Environ. Sci. Technol. 52 (2018) 3608–3614.

[10] Z. Xie, J. Zhou, J. Wang, C.P. François-Xavier, T. Wintgens, Novel Fenton-like catalyst γ-Cu-Al$_2$O$_3$-Bi$_{12}$O$_{15}$Cl$_6$ with electron-poor Cu centre and electron-rich Bi centre for enhancement of phenolic compounds degradation and H$_2$O$_2$ utilization:

[11] the synergistic effects of σ-Cu-ligand, dual-reaction centres and oxygen vacancies, Appl. Catal. B: Environ. 253 (2019) 28–40.

[11] Z. Xie, Z. Lyu, J. Wang, A. Li, P. François-Xavier Corvini, Ultrafine-Mn$_2$O$_3$@N-doped porous carbon hybrids derived from Mn-MOFs: dual-reaction centre catalyst with singlet oxygen-dominant oxidation process, Chem. Eng. J. 429 (2022), 132299.

[12] L. Lyu, L. Zhang, G. He, H. He, C. Hu, Selective H$_2$O$_2$ conversion to hydroxyl radicals in the electron-rich area of hydroxylated C-g-C$_3$N$_4$/CuCo–Al$_2$O$_3$, J. Mater. Chem. A 5 (2017) 7153–7164.

[13] L. Lyu, D. Yan, G. Yu, W. Cao, C. Hu, Efficient destruction of pollutants in water by a dual-reaction-center fenton-like process over carbon nitride compounds-complexed Cu(II)-CuAlO$_2$, Environ. Sci. Technol. 52 (2018) 4294–4304.

[14] C. Shan, H. Liu, M. Hua, B. Pan, Enhanced Fenton-like oxidation of As(III) over Ce-Ti binary oxide: a new strategy to tune catalytic activity by balancing bimolecular adsorption energies, Environ. Sci. Technol. 54 (2020) 5893–5901.

[15] Y. Sun, P. Tian, D. Ding, Z. Yang, W. Wang, H. Xin, J. Xu, Y.-F. Han, Revealing the active species of Cu-based catalysts for heterogeneous Fenton reaction, Appl. Catal. B: Environ. 258 (2019), 117985.

[16] Y. Sun, Z. Yang, P. Tian, Y. Sheng, J. Xu, Y.-F. Han, Oxidative degradation of nitrobenzene by a Fenton-like reaction with Fe-Cu bimetallic catalysts, Appl. Catal. B: Environ. 244 (2019) 1–10.

[17] L. Lyu, L. Zhang, Q. Wang, Y. Nie, C. Hu, Enhanced fenton catalytic efficiency of γ-Cu–Al$_2$O$_3$ by σ-Cu^{2+}–ligand complexes from aromatic pollutant degradation, Environ. Sci. Technol. 49 (2015) 8639–8647.

[18] L. Lyu, L. Zhang, C. Hu, M. Yang, Enhanced Fenton-catalytic efficiency by highly accessible active sites on dandelion-like copper–aluminum–silica nanospheres for water purification, J. Mater. Chem. A 4 (2016) 8610–8619.

[19] D. Malwal, P. Gopinath, Efficient adsorption and antibacterial properties of electrospun CuO-ZnO composite nanofibers for water remediation, J. Hazard Mater. 321 (2017) 611–621.

[20] Y. Yao, B. Gao, M. Inyang, A.R. Zimmerman, X. Cao, P. Pullammanappallil, L. Yang, Removal of phosphate from aqueous solution by biochar derived from anaerobically digested sugar beet tailings, J. Hazard Mater. 190 (2011) 501–507.

[21] P. Nazari, O. Nouri, Z. Xie, S.R. Setayesh, Z. Wei, Delafossite-alumina nanocomposite for enhanced catalytic wet peroxide oxidation of anionic pollutants, J. Hazard Mater. 417 (2021), 126015.

[22] R. Xiao, Z. Luo, Z. Wei, S. Luo, R. Spinney, W. Yang, D.D. Dionysiou, Activation of peroxymonosulfate/persulfate by nanomaterials for sulfate radical-based advanced oxidation technologies, Curr. Opin. Chem. Eng. 19 (2018) 51–58.

[23] J. Li, L. Yang, B. Lai, C. Liu, Y. He, G. Yao, N. Li, Recent progress on heterogeneous Fe-based materials induced persulfate activation for organics removal, Chem. Eng. J. 414 (2021), 128674.

[24] W.-T. Tsai, Human health risk on environmental exposure to Bisphenol-A: a review, J. Environ. Sci. Health C. 24 (2006) 225–255.

[25] G. Chen, H. Weng, Z. Wu, Y. Chen, P. Zhang, G. Ye, M. Lin, High-yield production of monolayer boron nitride nanosheets by cationic-surfactant-assisted solvothermal exfoliation for the ultrafast and selective separation of U(VI) from lanthanides, Sep. Purif. Technol. 278 (2021), 119645.

[26] A. Quintanilla, G. Vega, J. Carbajo, J.A. Casas, Y. Lei, K. Fujisawa, H. Liu, R. Cruz-Silva, M. Terrones, P. Miranzo, M.I. Osendi, M. Belmonte, J. Fernández Sanz, Understanding the active sites of boron nitride for CWPO: An experimental and computational approach, Chem. Eng. J. 406 (2021).

[27] T. Yamamoto, A. Yasuhara, H. Shiraishi, O. Nakasugi, Bisphenol A in hazardous waste landfill leachates, Chemosphere 42 (2001) 415–418.

[28] W.-D. Oh, S.-K. Lua, Z. Dong, T.-T. Lim, High surface area DPA-hematite for efficient detoxification of bisphenol A via peroxymonosulfate activation, J. Mater. Chem. A 2 (2014) 15836–15845.

[29] M.J. Frisch, G.W. Trucks, H.B. Schlegel, G.E. Scuseria, M.A. Robb, J.R. Cheeseman, G. Scalmani, V. Barone, G.A. Petersson, H. Nakatsuji, X. Li, M. Caricato, A.V. Marenich, J. Bloino, B.G. Janesko, R. Gomperts, B. Mennucci, H.P. Hratchian, J.V. Ortiz, A.F. Izmaylov, J.L. Sonnenberg, Williams, F. Ding, F. Lipparini, F. Egidi, J. Goings, B. Peng, A. Petrone, T. Henderson, D. Ranasinghe, V.G. Zakrzewski, J. Gao, N. Rega, G. Zheng, W. Liang, M. Hada, M. Ehara, K. Toyota, R. Fukuda, J. Hasegawa, M. Ishida, T. Nakajima, Y. Honda, O. Kitao, H. Nakai, T. Vreven, K. Throssell, J.A. Montgomery Jr, J.E. Peralta, F. Ogliaro, M.J. Bearpark, J.J. Heyd, E. N. Brothers, K.N. Kudin, V.N. Staroverov, T.A. Keith, R. Kobayashi, J. Normand, K. Raghavachari, A.P. Rendell, J.C. Burant, S.S. Iyengar, J. Tomasi, M. Cossi, J.M. Millam, M. Klene, C. Adamo, R. Cammi, J.W. Ochterski, R.L. Martin, K. Morokuma, O. Farkas, J.B. Foresman, D.J. Fox, Gaussian 16 Rev. C.01, Wallingford, CT, 2016.

[30] P.J. Stephens, F.J. Devlin, C.F. Chabalowski, M.J. Frisch, Ab Initio calculation of vibrational absorption and circular dichroism spectra using density functional force fields, J. Phys. Chem. C. 98 (1994) 11623–11627.

[31] A.V. Marenich, C.J. Cramer, D.G. Truhlar, Universal solvation model based on solute electron density and on a continuum model of the solvent defined by the bulk dielectric constant and atomic surface tensions, J. Phys. Chem. B 113 (2009) 6378–6396.

[32] Q.C. Tian L.U., Revealing Molecular Electronic Structure via Analysis of Valence Electron Density, 34 (2018) 503–513.

[33] T. Lu, F. Chen, Multiwfn: A multifunctional wavefunction analyzer, 33 (2012) 580–592.

[34] Z. Wang, Y. Liu, D.J. Martin, W. Wang, J. Tang, W. Huang, CuOx-TiO$_2$ junction: what is the active component for photocatalytic H$_2$ production? Phys. Chem. Chem. Phys. 15 (2013) 14956–14960.

[35] S. Tripathy, D. Bhattacharya, Rapid synthesis and characterization of mesoporous nanocrystalline MgAl$_2$O$_4$ via flash pyrolysis route, J. Asian Ceram. Soc. 1 (2018) 328–332.

[36] T. Tang, J. Zou, F. Luo, Z. Liu, S. Wu, F. Wang, D. Wang, J. Wu, Y. Qi, J. Li, F. Tian, Cu^{2+}-doped $BiOIO_3$ prepared by hydrothermal fabrication nanosheets for photocatalytic oxidation of gaseous mercury under visible light, Fuel 311 (2022), 122513.

[37] M.M. Hassan, W. Khan, A. Azam, A.H. Naqvi, Effect of size reduction on structural and optical properties of ZnO matrix due to successive doping of Fe ions, J. Lumin. 145 (2014) 160–166.

[38] L. Lyu, L. Zhang, C. Hu, Galvanic-like cells produced by negative charge nonuniformity of lattice oxygen on d-TiCuAl–SiO₂ nanospheres for enhancement of Fenton-catalytic efficiency, Environ. Sci.: Nano 3 (2016) 1483–1492.

[39] Q. Xiao, C. Zhan, Y. You, L. Tong, R. Wei, X. Liu, Preparation and thermal conductivity of copper phthalocyanine grafted boron nitride nanosheets, Mater. Lett. 227 (2018) 33–36.

[40] R.K.S. Anita Lagutschenkov, Philippe Maitre, Otto Dopfer, Structure and Infrared Spectrum of the Ag^+-Phenol Ionic Complex, J. Phys. Chem. A 114 (2010) 11053–11059.

[41] J. Cai, X. Zheng, W. You, L. Shen, Y. Zheng, Y. Cao, Y. Xiao, L. Jiang, Porous flake-like Al-rich MgAl2O4 endowed with Mg vacancies for efficient oxidative desulfurization, Appl. Catal. A-Gen. 623 (2021), 118238.

[42] A.-U.-R. Bacha, I. Nabi, H. Cheng, K. Li, S. Ajmal, T. Wang, L. Zhang, Photoelectrocatalytic degradation of endocrine-disruptor bisphenol A with significantly activated peroxymonosulfate by Co-$BiVO_4$ photoanode, Chem. Eng. J. 389 (2020), 124482.

[43] X. Liu, P. Shao, S. Gao, Z. Bai, J. Tian, Benzoquinone-assisted heterogeneous activation of PMS on Fe(3)S(4) via formation of active complexes to mediate electron transfer towards enhanced bisphenol A degradation, Water Res 226 (2022), 119218.

[44] L. Fu, H. Yang, Tailoring the electronic structure of mesoporous spinel γ-Al_2O_3 at atomic level: Cu-doped case, J. Phys. Chem. C. 118 (2014) 14299–14315.

[45] Z. Zheng, Y.H. Ng, Y. Tang, Y. Li, W. Chen, J. Wang, X. Li, L. Li, Visible-light-driven photoelectrocatalytic activation of chloride by nanoporous MoS_2@ $BiVO_4$ photoanode for enhanced degradation of bisphenol A, Chemosphere 263 (2021), 128279.

[46] M. Weng, M. Cai, Z. Xie, C. Dong, Y. Zhang, Z. Song, Y. Shi, M. Jin, Q. Wang, Z. Wei, Hydrodynamic cavitation-enhanced heterogeneous activation of persulfate for tetracycline degradation: synergistic effects, degradation mechanism and pathways, Chem. Eng. J. 431 (2022), 134238.

[47] X. Wang, J. Zhai, J. Yan, C. Gong, Y. Li, W. Zhu, Y. Luo, D. Yang, X. Gao, Highly Efficient Degradation of Carbamazepine by Activating Peroxymonosulfate with Lithium Cobaltite Cathode Powders Recovered from Spent Lithium-Ion Batteries.

[48] Y. He, L. Huang, B. Song, B. Wu, L. Yan, H. Deng, Z. Yang, W. Yang, H. Wang, Z. Liang, J. Luo, Defluorination by ion exchange of SO_4^{2-} on alumina surface: adsorption mechanism and kinetics, Chemosphere 273 (2021), 129678.

[49] Ž. Mitić, G.S. Nikolić, M. Cakić, P. Premović, L. Ilić, FTIR spectroscopic characterization of Cu(II) coordination compounds with exopolysaccharide pullulan and its derivatives, J. Mol. Struct. 924–926 (2009) 264–273.

[50] W. Guo, W. Hu, J. Pan, H. Zhou, W. Guan, X. Wang, J. Dai, L. Xu, Selective adsorption and separation of BPA from aqueous solution using novel molecularly imprinted polymers based on kaolinite/Fe₃O₄ composites, Chem. Eng. J. 171 (2011) 603–611.

[51] X. Li, X. Dai, J. Takahashi, N. Li, J. Jin, L. Dai, B. Dong, New insight into chemical changes of dissolved organic matter during anaerobic digestion of dewatered sewage sludge using EEM-PARAFAC and two-dimensional FTIR correlation spectroscopy, Bioresour. Technol. 159 (2014) 412–420.

[52] J. Fan, Z. Zhao, Z. Ding, J. Liu, Synthesis of different crystallographic FeOOH catalysts for peroxymonosulfate activation towards organic matter degradation, RSC Adv. 8 (2018) 7269–7279.

[53] M. Weng, M. Cai, Z. Xie, C. Dong, Y. Zhang, Z. Song, Y. Shi, M. Jin, Q. Wang, Z. Wei, Hydrodynamic cavitation-enhanced heterogeneous activation of persulfate for tetracycline degradation: synergistic effects, degradation mechanism and pathways, Chem. Eng. J. 431 (2022), 134238.

[54] C. Zhu, Y. Zhang, Z. Fan, F. Liu, A. Li, Carbonate-enhanced catalytic activity and stability of Co_3O_4 nanowires for (1)O_2-driven bisphenol A degradation via peroxymonosulfate activation: critical roles of electron and proton acceptors, J. Hazard Mater. 393 (2020), 122395.

[55] W. Huang, M. Brigante, F. Wu, C. Mousty, K. Hanna, G. Mailhot, Assessment of the Fe(III)-EDDS complex in Fenton-like processes: from the radical formation to the degradation of bisphenol A, Environ. Sci. Technol. 47 (2013) 1952–1959.

[56] G.M.R. Eli Finkelstein, Elmer J. Rauckman, Spin trapping. kinetics of the reaction of superoxide and hydroxyl radicals with nitrones, J. Am. Chem. Soc. 102 (1980) 4994–4999.

[57] K. Ranguelova, A.B. Rice, A. Khajo, M. Triquigneaux, S. Garantziotis, R. S. Magliozzo, R.P. Mason, Formation of reactive sulfite-derived free radicals by the activation of human neutrophils: an ESR study, Free Radic. Biol. Med. 52 (2012) 1264–1271.

[58] X. Dong, B. Ren, Z. Sun, C. Li, X. Zhang, M. Kong, S. Zheng, D.D. Dionysiou, Monodispersed $CuFe_2O_4$ nanoparticles anchored on natural kaolinite as highly efficient peroxymonosulfate catalyst for bisphenol A degradation, Appl. Catal. B: Environ. 253 (2019) 206–217.

[59] J. Du, B. Ren, Y. Liu, H. Ling, H. Zheng, S.H. Kim, D.D. Dionysiou, Efficient activation of peroxymonosulfate by magnetic Mn-MGO for degradation of bisphenol A, J. Hazard Mater. 320 (2016) 150–159.

[60] W. Li, P.-x Wu, Y. Zhu, Z.-j Huang, Y.-h Lu, Y.-w Li, Z. Dang, N.-w Zhu, Catalytic degradation of bisphenol A by CoMnAl mixed metal oxides catalyzed peroxymonosulfate: performance and mechanism, Chem. Eng. J. 279 (2015) 93–102.

[61] G.X. Huang, C.Y. Wang, C.W. Yang, P.C. Guo, H.Q. Yu, Degradation of bisphenol A by peroxymonosulfate catalytically activated with Mn1.8Fe1.2O4 nanospheres: synergism between Mn and Fe, Environ. Sci. Technol. 51 (2017) 12611–12618.

[62] X. Li, Z. Wang, B. Zhang, A.I. Rykov, M.A. Ahmed, J. Wang, Fe Co3−O4 nanocages derived from nanoscale metal–organic frameworks for removal of bisphenol A by activation of peroxymonosulfate, Appl. Catal. B: Environ. 181 (2016) 788–799.

[63] Z. Shi, C. Jin, R. Bai, Z. Gao, J. Zhang, L. Zhu, Z. Zhao, T.J. Strathmann, Enhanced transformation of emerging contaminants by permanganate in the presence of redox mediators, Environ. Sci. Technol. 54 (2020) 1909–1919.

[64] J. Li, Y. Zhou, J. Jiang, S.-Y. Pang, Y. Gao, Y. Yang, G. Liu, J. Ma, C. Jiang, L. Wang, Transformation of phenolic compounds by peroxymonosulfate in the presence of iodide and formation of iodinated aromatic products, Chem. Eng. J. 335 (2018) 855–864.

[65] R.A. Torres-Palma, J.I. Nieto, E. Combet, C. Petrier, C. Pulgarin, An innovative ultrasound, Fe^{2+} and TiO₂ photoassisted process for bisphenol A mineralization, Water Res 44 (2010) 2245–2252.

[66] J. Poerschmann, U. Trommler, T. Gorecki, Aromatic intermediate formation during oxidative degradation of Bisphenol A by homogeneous sub-stoichiometric Fenton reaction, Chemosphere 79 (2010) 975–986.

[67] X. Xu, S. Zong, W. Chen, D. Liu, Comparative study of Bisphenol A degradation via heterogeneously catalyzed H2O2 and persulfate: reactivity, products, stability and mechanism, Chem. Eng. J. 369 (2019) 470–479.

[68] Q. Wang, C. Liu, D. Zhou, X. Chen, M. Zhang, K. Lin, Degradation of bisphenol a using peroxymonosulfate activated by single-atomic cobalt catalysts: different reactive species at acidic and alkaline pH, Chem. Eng. J. 439 (2022), 135002.